

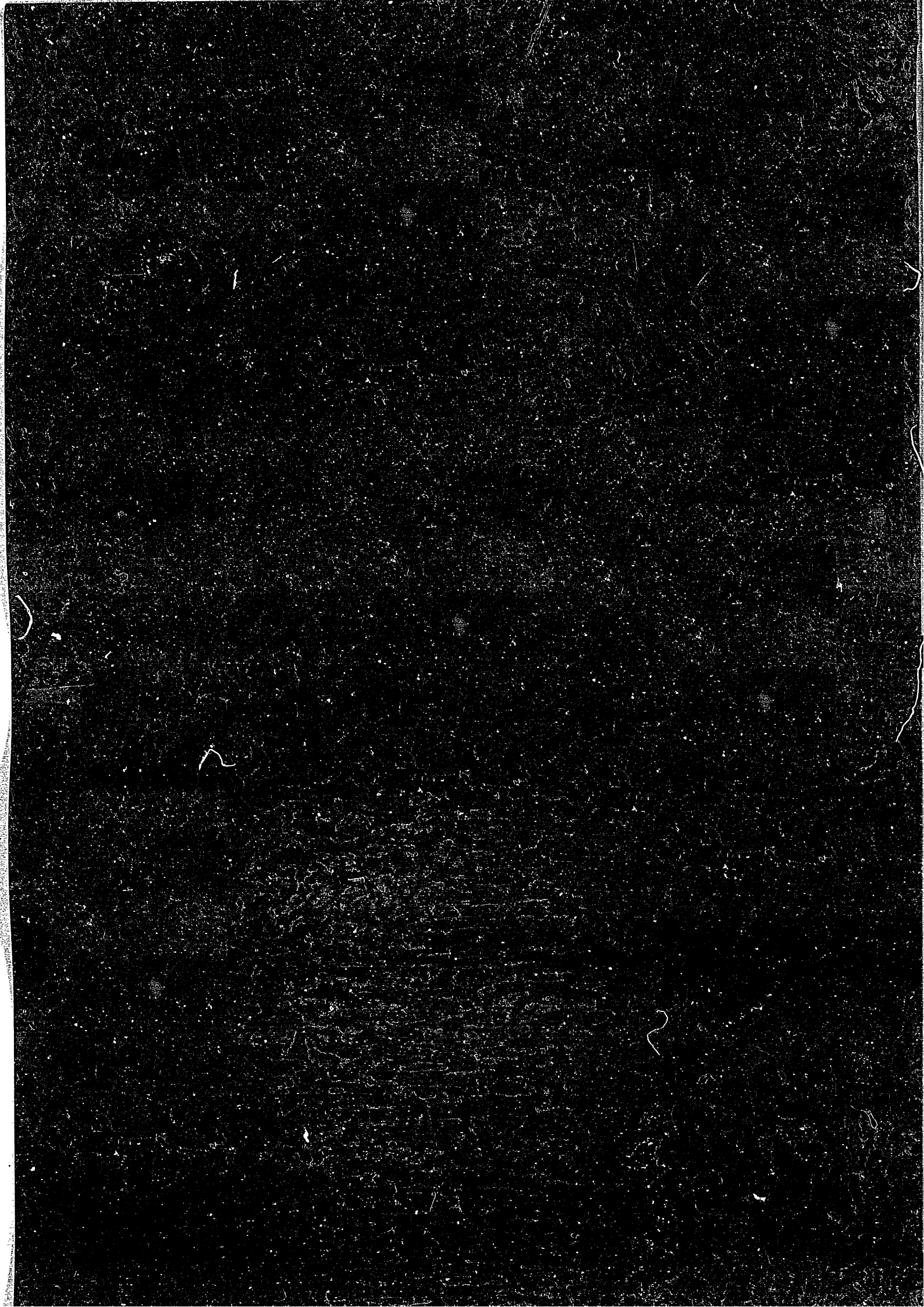
IPPJ-AM-40

**LOW-ENERGY SPUTTERINGS
WITH
THE MONTE CARLO PROGRAM ACAT**

Y. YAMAMURA AND Y. MIZUNO

**INSTITUTE OF PLASMA PHYSICS
NAGOYA UNIVERSITY**

NAGOYA, JAPAN



**LOW-ENERGY SPUTTERINGS WITH
THE MONTE CARLO PROGRAM ACAT[†]**

Yasunori YAMAMURA* and Yoshiyuki MIZUNO*

**Institute of Plasma Physics, Nagoya University
Chikusa-ku, Nagoya 464, Japan**

May 1985

***Permanent address: Okayama University of Science
Ridai-cho, Okayama 700, Japan**

**[†]This work was carried out under the Collaborating Research Program at the Institute
of Plasma Physics, Nagoya University, Nagoya.**

This document is prepared as a preprint of compilation of atomic data for fusion research sponsored fully or partly by the IPP/Nagoya University. This is intended for future publication in a journal or will be included in a data book after some evaluations or rearrangements of its contents. This document should not be referred without the agreement of the authors. Enquiries about copyright and reproduction should be addressed to Research Information Center, IPP/Nagoya University, Nagoya, Japan.

Abstract

The Monte Carlo program ACAT was developed to determine the total sputtering yields and angular distributions of sputtered atoms in physical processes. From computer results of the incident-energy dependent sputterings for various ion-target combinations the mass-ratio dependence and the bombarding-angle dependence of sputtering thresholds was obtained with the help of the Matsunami empirical formula for sputtering yields. The mass-ratio dependence of sputtering thresholds is in good agreement with recent theoretical results. The threshold energy of light-ion sputtering is a slightly increasing function of angle of incidence, while that of heavy-ion sputtering has a minimum value near $\theta = 60^\circ$.

The angular distributions of sputtered atoms are also calculated for heavy ions, medium ions, and light ions, and reasonable agreements between calculated angular distributions and experimental results are obtained.

I. Introduction

The low-energy sputtering is one of the most important problems for the plasma surface interactions, because the sputtering is one of the main impurity release processes from the first wall of tokamaks. The energy of ions and neutral atoms near the first wall is less than 100 eV. There is no theoretical formula which can predict the sputtering yields for such low-energy ions.

Since the Sigmund theoretical works on sputtering¹, numerous publications have been published. Analytical studies based on the linearized transport equation should introduce some special simplifying assumptions. For very low-energy sputtering, the most unrealistic assumption is to neglect the boundary effect. Furthermore it should be noted that the transport equation includes the infinite number of the binary collisions. When the ion energy is in the near-threshold region, the collision number is limited due to the finiteness of the target medium and the large mean free path of the low-energy recoil which becomes comparable to the average lattice constant.

In view of these difficulties, computer simulations of the collision processes near the solid surface appear worthwhile for studying the low-energy sputtering. At present there are two methods of computer simulations on atomic collisions in solids, i.e., the Monte Carlo method^{2,3,4} and the molecular dynamics method^{5,6}. The molecular dynamics method is the powerful method for low-energy atomic collisions in solids and can treat the simultaneous collisions of moving atoms with low-energies. The application of this method to the polycrystalline target or the amorphous target, however, is time-consuming. Since the full molecular dynamics cannot be applied to the amorphous target, one should calculate the sputtering yields for various crystal axes and after this one should average them. The Monte Carlo method is more convenient for practical applications. However, the Monte Carlo simulation is usually based on the binary collision approximation which is a rough approximation for the collision of very low-energy ions, and so one needs some idea in simulating sputtering processes by the Monte Carlo method.

Up to now we have several Monte Carlo simulation programs, i.e., MARLOWE⁷, TRIM.SP⁸, ACAT³, and Ishitani-Shimizu codes⁴. In the first three programs the scattering angle at each collision is a function of the impact parameter and is numerically calculated using the screened Coulomb potential, while Ishitani and Shimizu used the differential cross section at each collision and the concept of the mean free path which is often used in the neutron slowing down problem.

The MARLOWE code was originally developed to simulate atomic collisions in a single crystal solid. In order to apply this code to the amorphous target, the crystal axis should be rotated randomly in three dimensions before each collision.

On the other hand, the TRIM code² has been designed to simulate atomic collisions in the random target assuming the fixed mean free path with the value $N^{-1/3}$ (N is the number density of target atom) and the impact parameter is randomly selected at each collision. Recently Biersack and Eckstein⁸ modified the previous existing TRIM code in order to follow the recoil atoms as well as ions. This modified TRIM code is named as TRIM.SP. In the TRIM.SP program the simultaneous scattering events are effectively taken into account.

In the ACAT program an amorphous target is simulated employing the so-called cell model, in which a target atom is randomly selected in a simple cubic cell with a lattice constant $R_0 = N^{-1/3}$. In the MARLOWE and ACAT codes, the position of an atom is uniquely determined, and the impact parameter is calculated through the relation between the direction of the moving particle and the position of the target atom. Therefore the too-low-energy particle cannot fly any more automatically because the apsidal distance is too large. Because of the simplicity of the TRIM and ACAT codes, these two codes are by more than ten times faster than the MARLOWE code. As a matter of course, both the TRIM and the ACAT codes cannot be applied to a single-crystal target.

In this report we have improved the previous existing ACAT code³ so as to treat more reasonably the surface scatterings of leaving particles from the solid surface. The effect of the surface scattering of outgoing particles is very important for angular distributions of sputtered atoms and reflected ions, especially in the case of grazing angles of incidence. The main concern of this report is to show the validity of the ACAT code. For this purpose we calculate the total sputtering yields and associated angular distributions at normal incidence and oblique incidence. As an application sputtering thresholds will be derived from calculated sputtering yields with the help of the Matsunami empirical formula which was proposed by the Sputtering Data Compilation Group under the joint research program at Institute of Plasma Physics, Nagoya University.⁹

II. The ACAT Program

The ACAT program was developed to simulate the atomic collisions in an amorphous target within the framework of the binary collision approximation, and in the ACAT program the target atom is randomly distributed in each unit cubic cell of which the lattice constant is $R_0 = N^{-1/3}$. The particle is assumed to move only along the straight-line segments, these being the asymptotes of its path in the laboratory (L) system.

The atomic collisions are considered to be composed of an elastic part and the

electron excitation part. The trajectories of two particles interacting according to a conservative central repulsive force are shown in Fig. 1, which defines several terms of present interest. The equation of motion which describe these trajectories can be manipulated in the usual manner to yield the scattering angle in the center-of-mass (CM) system⁸

$$\Theta = \pi - 2p \int_{r_0}^{\infty} dr [r^2 g(r)]^{-1} \quad (1)$$

and time integral

$$\tau = (r_0^2 - p^2)^{-1/2} - \int_{r_0}^{\infty} dr [\{g(r)\}^{-1} - (1 - p^2/r^2)^{-1/2}] , \quad (2)$$

where

$$g(r) = [1 - p^2/r^2 - V(r)/E_r]^{1/2}, \quad (3)$$

p is the impact parameter, E_r is the relative kinetic energy, r is the interatomic separation, $V(r)$ is the interatomic potential, and r_0 is the apsidal distance defined by $g(r) = 0$. The relative kinetic energy is

$$E_r = \frac{A}{A+1} E_0 , \quad (4)$$

where E_0 is the incident kinetic energy of the projectile and $A = M_2/M_1$ is the ratio of the mass of the target atom M_2 and that of the projectile M_1 . In the ACAT code, the CM scattering angle and the time integral are initially calculated by four-point Gauss-Legendre quadrature according to Everhart's method¹⁰ and are stored in the two-dimensional matrix. The scattering angle and the time integral at each collision are evaluated with the help of the two-dimensional interpolation formula.

In constructing the trajectory of the projectile, one has to note that the deflection point is shifted backward in the L system by an amount Δx_1 , which is shown in Fig. 1. For the trajectory of the recoil atom the starting point is shifted forward by an amount Δx_2 from the initial position of the target atom. The explicit expressions of Δx_1 and Δx_2 are as follows:

$$\Delta x_1 = [2\tau + (A-1) p \tan \frac{\Theta}{2}] / (1 + A), \quad (5)$$

$$\Delta x_2 = p \tan \frac{\Theta}{2} - \Delta x_1 . \quad (6)$$

The interatomic potential $V(r)$ can be chosen in the ACAT program from six options, i.e., the Moliere potential¹¹, the Kr-C potential¹², the Ziegler potential¹³, the

Lenz-Jensen (LJ) potential¹⁴, the aLJ potential¹⁵, and the aMLJ potential¹⁶ (Table 1). In the present calculations we employed the Moliere approximation to the Thomas-Fermi potential

$$V(r) = \frac{Z_1 Z_2 e^2}{r} \Phi(r/a) , \quad (7)$$

where

$$\Phi(x) = 0.35 \exp(-0.3x) + 0.55 \exp(-1.2x) + 0.10 \exp(-6.0x) \quad (8)$$

a is the screening length, and Z_1 and Z_2 are the atomic numbers of the projectile and the target atom, respectively.

In the ACAT program the electronic energy loss ΔE_e can be chosen from three options: 1) The trajectory-dependent energy loss model (non-local). This model is independent of the impact parameter, i.e.,

$$\Delta E_e = L_m N S_e(E) , \quad (9)$$

where L_m is the distance between collisions, and $S_e(E)$ is the electronic stopping cross section. For hydrogen we used the four-parameter fitting formula¹⁷ of the electronic stopping cross section which was originally proposed by Varelas and Biersack¹⁸

$$S_e(E)^{-1} = (S_{LOW}^H)^{-1} + (S_{HIGH}^H)^{-1} , \quad (10)$$

where

$$S_{LOW}^H = A_1 E^{0.45} , \quad (11)$$

$$S_{HIGH}^H = (A_2/E) \ln [1 + (A_3/E) + A_4] ,$$

and four parameters in Eq. (11) are stored in the ACAT code.

For helium isotopes we used the five-parameter fitting formula^{18,19} of the Ziegler table

$$S_e(E)^{-1} = (S_{LOW}^{He})^{-1} + (S_{HIGH}^{He})^{-1} , \quad (12)$$

where

$$S_{LOW}^{He} = A_1' \bar{E} A_2' , \quad (13)$$

$$S_{HIGH}^{He} = (A_3'/\bar{E}) \ln [1 + (A_3'/\bar{E}) + A_5' \bar{E}] , \quad (14)$$

\bar{E} is the He energy in keV, and these five parameters are stored in the ACAT code.

For other heavier ions, the Lindhard-Scharff energy loss model is employed,¹⁹ i.e.,

$$S_e(E) = K_L E^{1/2}, \quad (15)$$

where the Lindhard electronic stopping coefficient K_L is given as

$$K_L = \frac{1.212Z_1^{7/6} Z_2}{(Z_1^{2/3} + Z_2^{2/3})M_1^{1/2}} [(eV)^{1/2} \cdot \text{\AA}^2]. \quad (16)$$

2) The Oen-Robinson energy loss model (local).²⁰ This model depends on the impact parameter p through the apsidal distance in the binary collision, i.e.,

$$\Delta E_e = \frac{0.045}{\pi a^2 (1 - \alpha)} S_e(E) \exp[-0.3r_0(p,E)/p], \quad (17)$$

where the factor $(1 - \alpha)$ is a correction term due to the finiteness of the impact parameter in the solid, and $S_e(E)$ is the electronic stopping cross section which is given by Eqs. (10), (12) and (15) for hydrogen, helium, and heavier ions, respectively. The explicit expression of α is as follows:

$$\alpha = (1 + 0.18611R_0/a) \exp(-0.18611R_0/a). \quad (18)$$

3) The mixed model. The third consists of a combination of the previous non-local model and the Oen-Robinson (OR) local model. In the computer simulation of sputtering phenomena recoil atoms with very low-energies are moving in the solid, and their free paths are too short to apply the non-local model for the electronic energy loss, because the non-local model is the macroscopic representation of the electronic energy loss process. In the mixed model of the ACAT code, for $\lambda(E) < 5R_0$, the electronic energy loss is calculated by the OR local model, and for $\lambda(E) > 5R_0$ it is estimated by non-local model. Here $\lambda(E)$ is the effective mean-free-path which is given as $\lambda(E) = 1/\pi N b^2$, where b is the collision diameter defined by $b = r_0(0,E)$.

The procedure of searching the collision partner of the ACAT program is very simple. Let the projectile move in the direction e_p . The notation "projectile" is used here for the ion or any recoil atom moving in solids. In the ACAT program, the projectile flies from the position R step by step by an amount Δx along the direction e_p (see Fig. 2). The position of the projectile R_n after n times step is $R + n\Delta x e_p$, and the unit cell belonging to R_n is easily determined dividing each component of R_n by the average lattice constant R_0 . If the unit cell of R_n is different from that of the original position R , a target atom is produced randomly in a new unit cell using three random variables, and this target atom is a collision partner.

Let the position of the target atom be R_A which is shown in Fig. 2. Then, the impact parameter p is given as

$$p = \frac{|(R_A - R) \times e_p|}{|R_A - R|} \quad (19)$$

The CM scattering angle and the time integral for this collision are easily obtained from the pre-calculated two-dimensional matrix.

In the ACAT code we introduced two different coordinates. The one is the absolute coordinate fixed to the target, where the x-y plane is on the solid surface, and the direction of the z axis is opposite to the surface normal. The other is the moving coordinate which is fixed to the moving projectile, where the direction of the z -axis is equal to e_p . In Fig. 3 these two coordinate are schematically shown in the spherical trigonometry. The X, Y, and Z in Fig. 3 correspond to the x, y, and z axes of the absolute coordinate, while the A, B, and P to the x, y, and z axes of the moving coordinates. The direction e_A of the A axis is chosen to be

$$e_A = \frac{e_p \times [e_p \times (R_A - R)]}{p} \quad (20)$$

and the direction e_B of the B axis is $[e_A \times e_p]$. The direction S in the P-A plane is that of the scattered projectile after the collision, and $\hat{\theta}$ is the scattering angle in the L system which is given as

$$\hat{\theta} = \tan^{-1} \frac{A \sin \theta}{1 + A \cos \theta} \quad (21)$$

The direction e'_S of the projectile after collision is represented by

$$e'_S = \begin{pmatrix} \sin \hat{\theta} \\ 0 \\ \cos \hat{\theta} \end{pmatrix} \quad (22)$$

in the moving coordinate. Transforming the bases of the moving coordinate into those of the absolute coordinate yields the direction S in the absolute system which is obtained as follows:

$$e_S = \hat{T} e'_S, \quad (23)$$

where $\hat{T} = (e_A, e_B, e_p)$ is the inverse matrix of the transformation matrix between two bases.

The surface scattering with the target atom at the topmost layer, which is suffered by an incoming or outgoing particle, is very important for the angular distributions of reflected particles and sputtered recoil atoms, especially for oblique incidence. In the ACAT program the procedure of searching the collision

partner of the particle moving in the vacuum is two-dimensional. In other words, the projected position moves on the solid surface as the projectile does in the vacuum as if a shadow of an airplane moves on the earth surface. Figure 4 shows how to search the collision partner of an outgoing particle, where the positions $\bar{\mathbf{R}}$ and $\bar{\mathbf{R}}_n$ are the projected ones of \mathbf{R} and \mathbf{R}_n , respectively. Similarly to the searching procedure in the bulk we can determine a new unit cell which the position $\bar{\mathbf{R}}_n$ belongs to and get the candidate for the collision partner. In the case of the bulk the target atom obtained like this is always a collision partner, but for surface scattering we should check whether the binary collision approximation is allowed or not. Inside the solid the roughness of the binary collision approximation is smeared out statistically due to subsequent collisions. In the case of the surface scattering of the outgoing particle with the surface atom its total scattering angle - which is measured from the incident direction - is always enlarged due to the surface scattering, and the roughness of the binary collision approximation will be enhanced if any target atom in the new unit cell is allowed as a collision partner. In the ACAT program the target atom in a new unit cell is accepted as a collision partner if $(\mathbf{R} - \mathbf{R}_A) \cdot \mathbf{e}_p - \Delta x_1 + R_0 |\mathbf{e}_p \times \mathbf{e}_z| > 0$, where the last term of this inequality comes from randomness of the surface atom, and \mathbf{e}_z is the direction of the z axis of the absolute coordinate fixed to the target. This procedure of searching the collision partner is repeated until the impact parameter between the leaving particle and the surface atom is larger than R_0 , and this leaving particle with the large impact parameter is regarded as escaping the repulsive potential region of the solid surface.

The surface binding energy U_s has a significant influence on the total sputtering yields, and also on the angular and energy distributions of sputtered atoms. As the surface binding energy, we have used the sublimation energy E_s data which are stored in the ACAT program. The surface binding energy acts in the form of a planar attractive potential upon the atoms which are leaving the surface, and results in a refraction or even a reflection back into the solid, depending on energy and angle of the leaving atom.

For the cascade development we have used three parameters, i.e., the bulk binding energy E_B , the displacement energy E_d , and the minimum energy E_c until which the cascade continues to develop. These three parameters are the input data. Let us consider a collision from which the original projectile emerges with kinetic energy E_1 after transferring kinetic energy T to the target atom. The target atom is displaced if its energy exceeds a sharp threshold energy E_d . It may be required at the same time to overcome a bulk binding energy: $E_B \leq E_d$. If $T > E_d$, the target atom is added to the cascade with the kinetic energy

$$E_2 = T - E_B . \quad (24)$$

The cascade develops continuously so long as their energies exceed a preassigned value E_c . In Fig. 5 a typical example of the cascade development in solids is shown shown, where 10 keV Ar^+ ions are bombarded on a copper target.

Once a new recoil atom is ejected from its original site a vacancy will be left even for the case of replacement collision which takes place when $T > E_d$ and E_l is less than the lesser of E_c and E_d , because this trapped projectile still has kinetic energy which must be dissipated before it gets the well-defined position. The time required for this energy dissipation will exceed the time needed to generate the cascade. Roughly speaking, the bulk binding energy will be of the order of the vacancy formation energy, i.e., about 1 eV for fcc metals and about 3 eV for bcc metals.

There are several models for the bulk binding energy in the simulation of sputtering processes. However, bulk binding energies are of little influence on the sputtering results,⁸ because E_B is usually small compared with the transferred energy at high energy bombardment. Moreover most sputtered atoms originate in the surface layer where the binding energy E_B is not equal to the vacancy formation energy in the bulk. On the other hand sputtering phenomena is in a sense a transient one which is different from other radiation phenomenon such as radiation damage where the displacement energy E_d is of the order of 25 eV. The displacement energy is the minimum energy required to produce the stable Frenkel pair. Since almost all sputtered atoms originate in the surface layer, we need not use the criterion whether the recoil atom get the kinetic energy enough for the stable Frenkel pair or not. Then, in the case of simulating sputtering process the following simple model is used in the ACAT program:

$$E_B = 0, E_c = E_s, E_d = E_s, U_s = E_s. \quad (25)$$

III. Results and Discussions

In this report the ACAT program has been applied to calculating low-energy sputtering yields and the associated angular distributions of sputtered atoms for normal incidence and oblique incidence. In order to study the mass-ratio dependence of sputtering thresholds, first of all, the energy dependence of sputtering yields is calculated for various ion-target combinations. Secondly, in order to obtain the bombarding-angle dependence of sputtering thresholds, the bombarding-angle dependence of sputtering yields are simulated for very low-energy ions. As the ion-target combinations we adopted H+Ni, Ar+Cu, and Hg+Ni combinations which correspond to light-ion, medium-ion, and heavy-ion sputterings, respectively. In this report we classified the ion-target combination into three categories from the mass-ratio

between the atomic mass of target atom and that of projectile, i.e.,

- 1) light-ion sputtering ($M_2/M_1 > 10$),
- 2) medium-ion sputtering ($10 > M_2/M_1 > 1$),
- 3) heavy-ion sputtering ($M_2/M_1 < 1$).

The border line between light-ion sputtering and medium-ion sputtering is not clearly defined.

Weissmann and Behrisch²¹ attempted to separate the sputtering mechanism into two parts (see Fig. 6): one due to collision cascades created by incoming ions directly and the other due to collision cascades generated by ions interior of the solid, i.e.,

$$Y_{\text{tot}} = Y_{\text{I}} + Y_{\text{II}} \quad (26)$$

The former process is the main sputtering mechanism for heavy-ion sputtering, while the latter mechanism is dominant for light-ion sputtering. The high-energy medium-ion sputtering behaves as heavy-ion sputtering, while the very low-energy medium-ion sputtering will obey the same sputtering mechanism as light-ion sputtering.

3.1 Low-energy sputtering yields and sputtering thresholds at normal incidence

In order to obtain the preliminary descriptions of low-energy sputtering yields, the empirical formula have been proposed by Bohdansky²² and Yamamura et al.²³ These formulae have the following two features: 1) When the ion energy is so high that the recoil density can be described in the asymptotic form, these empirical formulae become equal to the original Sigmund formula¹. 2) These formulae include the effect of sputtering thresholds which are determined empirically.

About 25 years ago, Harrison and Magnuson²⁴ investigated the sputtering thresholds for a crystalline target based on the Silsbee chain model. Their theory cannot be applied to heavy-ion sputtering, because their formula was derived assuming a single collision reorientation to the Silsbee chain. Considering the main process leading to threshold sputtering of light ions, Behrisch et al.²⁵ have derived intuitively the threshold energy of light-ion sputtering

$$E_{\text{th}} = \frac{U_s}{\gamma(1 - \gamma)} \quad (27)$$

where $\gamma = 4M_1M_2/(M_1+M_2)^2$ is the energy transfer factor.

Under these circumstances it is very important to investigate sputtering thresholds for various ion-target combinations. For this purpose, in this report, the mass ratio dependence and the bombarding angle dependence of sputtering thresholds have been studied using the present ACAT program.

Figures 7 and 8 show the energy dependences of sputtering yields for various ion-target combinations, where the ACAT results are compared with measured data. In Table 2 we show the screening lengths and the surface binding energies used in the present calculations and in Table 3 the contributions of Mechanism 1 (Y_I), Mechanism 2 (Y_{II}), and primary recoil atoms (Y_p) are shown explicitly for typical three energies, where N_0 is the number of primary ions. For too-low-energy ions the difference between Y_I and Y_{II} is not clear, because the collision events take place only near the surface. The agreement between ACAT results and measured data is very good. In the case of very low-energy light-ions and medium-ions the majority of sputtered atoms are primary recoil atoms, while for very low-energy heavy-ions primary recoil atoms cannot be sputtered. As the incident energy becomes higher, the contribution of Mechanism 1 becomes more important for medium-ion sputtering, while Mechanism 2 is dominant for light-ion sputtering even for high energy ions.

It is a time-consuming problem to determine the threshold energy directly from the computer simulation, because we need a large number of primary ions for the near-threshold sputtering. In order to avoid this difficulty, here, we use the following empirical formula^{3,9}:

$$Y = \Lambda \frac{\alpha(M_2/M_1)}{U_s} S_n^*(E) [1 - (E/E_{th})^{1/2}]^n, \quad (28)$$

which includes the effect of sputtering thresholds, where E_{th} is the threshold energy at normal incidence, Λ is an energy-independent constant, $\alpha(M_2/M_1)$ is an energy-independent function of the mass ratio M_2/M_1 , and $S_n^*(E)$ is the effective nuclear stopping cross section which is defined as

$$S_n^*(E) = \frac{S_n(E)}{1 + 0.35 U_s s_e(\epsilon)}. \quad (29)$$

Here, $S_n(E)$ is the nuclear stopping cross section, and $s_e(\epsilon)$ is the LSS reduced electronic stopping cross section which corresponds to Eq. (15). The nuclear stopping cross section $S_n(E)$ is calculated using the Ziegler universal nuclear cross section which is represented in the LSS reduced energy ϵ ¹⁷

$$s_n(\epsilon) = \frac{0.5 \ln(1 + 1.1383\epsilon)}{\epsilon + 0.013218\epsilon^{0.21226} + 0.19594\epsilon^{0.5}}. \quad (30)$$

Some rearrangement of Eq. (28) yields the following simple equation:²⁶

$$Y^* = A(E^{1/2} - E_{th}^{1/2}), \quad (31)$$

where A is an energy-independent constant, and

$$Y^* = E^{1/2} \left(\frac{Y}{S_n^*(E)} \right)^{1/n} \quad (32)$$

Equation (31) tells us that if one plots Y^* against $E^{1/2}$ we can determine the threshold energy from the point of intersection of Y^* with the $E^{1/2}$ axis.

In Ref 3 $n=2$ was used as the exponent of the square bracket in Eq. (28), but recent works revealed that $n=2.8$ is better than $n=2$ ⁹. The linearity of Y^* is shown in Figs. 9 and 10. The yield data in Fig. 9 are ACAT results, and the solid lines in Figs. 7 and 8 correspond to the solid lines in Fig. 9. The threshold energies are also determined from measured data in a similar manner, which is shown in Fig. 10. The exponent $n=2$ always gives the larger threshold energies than the exponent $n=2.8$, of which the threshold energies are coincident with those of Eq. (27) for light-ion sputtering. Then in the following discussions we employ $n=2.8$ as the exponent of the square bracket in Eq. (28). Table 4 shows threshold energies which are obtained from Eq. (4) using the ACAT data, and they are plotted as a function of the mass ratio M_2/M_1 in Fig. 11. The solid line in Fig. 11 is

$$E_{th}/U_s = 0.214 + 4.77(M_1/M_2)^{0.567} + 0.256(M_2/M_1). \quad (33)$$

In Fig. 12 we compare the ACAT threshold energies with the experimental threshold energies which are obtained from Eq. (31) using the measured data. The $n=2$ curve corresponds to ACAT threshold energies which are obtained from Eqs. (31) and (32) with the exponent $n=2$ (see Table 4), while the $n=2.8$ curve corresponds to Eq. (33).

3.2 Few collision approach for threshold sputtering at normal incidence

Referring the computer works on very low-energy sputtering, Yamamura and Bohdansky²⁷ picked up some possible collision sequences for near-threshold sputtering which are shown in Fig. 13 and 14. In the case of Mechanism 1 the primary recoil atom leading to the emission process is produced at the first collision of the projectile with surface atom, while in Fig. 14 the primary recoil atom leading to sputtering is created after a few collisions. Mechanism 1 and Mechanism 2 of these figures correspond to those of Fig. 6. Additional distinctions, A, B, C, and D in Figs. 13 and 14 correspond to different number of collisions which a sputtered atom experiences before ejection.

Assuming that any configuration of each target atom is allowed for threshold sputtering, they derived a simple analytic expression for the "threshold energy" of each mechanism in Figs. 13 and 14. Each mechanism has its own "threshold energy", and the lowest "threshold energy" is considered as the real threshold energy for the special ion target combination. Tables 5 and 6 show analytic expressions for the "threshold energies" of

each mechanism listed in Figs. 13 and 14, where m is the collision number at the deeper layer than the topmost layer, θ_1 is the CM scattering angle at the first collision, $\hat{\theta}$ and $\hat{\hat{\theta}}$ are the scattering angles in the L system which are represented in terms of θ_1

$$\hat{\theta} = \tan^{-1} \frac{\sin\theta_1}{\mu + \cos\theta_1}, \quad (34)$$

$$\hat{\hat{\theta}} = \tan^{-1} \frac{\mu \sin\theta_1}{1 + \mu \cos\theta_1} \quad (35)$$

with the definition of $\mu = M_1/M_2$, and α is the angle of incidence.

Formula for Mechanism 1D and Mechanism 2C include the unknown parameter m , i.e., the collision number m . For light ions, the m -dependence of the threshold energy is very weak. From theoretical point of view, it is very difficult to determine this collision number m precisely, because m is the effective number of the binary collisions which the moving particle experiences near the surface. According to computer simulation of low-energy sputtering, this number is very small, since the collision events available for threshold sputtering do not occur in the deeper layer.

Comparing theoretical threshold energy with experimental values Yamamura and Bohdanský choose $m=2$ as the collision number included in theoretical formulae. Substituting $m=2$ and $\alpha=0$ into the formulae of Mechanism 1D and Mechanism 2C, we have simple formulae for threshold energy at normal incidence

$$E_{th} = \begin{cases} \left(\frac{4}{3}\right)^6 \frac{U_s}{\gamma} & M_1 > M_2 \\ \frac{U_s}{\gamma} \left(\frac{2M_1 + 2M_2}{M_1 + 2M_2}\right)^6 & M_1 < M_2 \end{cases} \quad (36)$$

In Fig. 15 we compare theoretical formula Eq. (36) with experimental threshold energies which are determined from Eq. (31). The solid line means the present theoretical values, and other marks means experimental threshold energies. The agreement between theory and experiment is very good.

3.3 Angular distributions of sputtered atoms at normal incidence

Using the ACAT program, the angular distribution of sputtered atoms is calculated for low-energy ions at normal incidence. As the ion-target combinations we choose Hg^+-Ni , Ar^+-Cu , and H^+-Ni which correspond to heavy-ion, medium-ion, and light-ion sputterings, respectively. In Fig. 16 we draw the angular distributions of sputtered atoms for $Hg^+ \rightarrow Ni$, where incident energies are 100 eV and 1000 eV. The angular distribution of 1000 eV $Hg^+ \rightarrow Ni$ is nearly the cosine-distribution, while that of 100eV $Hg^+ \rightarrow Ni$

shows the strong under-cosine distribution. According to a few-collision model²⁷, possible sputtering mechanisms are Mechanism 1D and Mechanism 1C for 100eV Hg⁺-Ni. Sputtering yield of Mechanism 1C is larger than that of Mechanism 1D, because the former mechanism is the four collision process. The preferential angle of this process is about 55°, while the preferential angle of the ACAT distribution is about 55°.

Fig. 17 shows the angular distributions of sputtered atoms for 50eV Ar⁺→Cu and 100eV Ar⁺→Cu, while those of 1000eV Ar⁺→Cu are drawn in Fig. 18. As the incident energy becomes lower, the angular distribution become the under-cosine distribution. The angular distribution of 50eV Ar⁺→Cu is very similar to that of 100eV Hg⁺→Ni. The possible mechanisms are Mechanisms 2C, 2B, and 1D for 50eV Ar⁺→Cu, and the largest sputtering yield comes from Mechanism 2B of which the preferential angle is about 56°. The agreement between theory and simulation is very good.

Fig. 19 shows the angular distributions of sputtered atoms for light-ion sputtering, (i.e., 100eV H⁺→Ni, 450eV H⁺→Ni, and 1000eV H⁺→Ni. The angular distributions of high energy ions have the dip at the surface normal, while that of the near-threshold energy has a peak at the surface normal. For 100 eV H⁺ ion the possible mechanisms are 2C, 2B, and 2A whose preferential ejection angle is nearly 0° according to Yamamura and Bohdanský theory.

3.4 Low-energy sputtering yields and sputtering thresholds at oblique incidence

In Fig. 20 we shows the bombarding-angle (α) dependence of sputtering yields for low-energy ions, where as the ion-target combinations we choose Hg⁺-Ni, Ar⁺-Cu, and H⁺-Ni which correspond to heavy-ion sputtering, medium-ion sputtering, and light-ion sputtering, respectively. It is very interesting that in the case of Hg⁺→Ni, even if the ion energy is lower than the threshold energy at normal incidence, a finite number of target atoms are sputtered for oblique incidence and that the low-energy heavy-ion sputtering yields are strong increasing functions of the angle of incidence up to $\alpha = 60^\circ$. In the case of light-ion sputtering such as H⁺→Ni, the sputtering yield of the near-threshold ions is nearly constant up to 60°, and it drops rapidly for $\alpha > 70^\circ$ due to surface scattering.

For not-too-oblique incidence the parameter $\alpha(M_2/M_1)$ of Eq. (28) is not a function of incident energy, but of angle of incidence. For grazing angle of incidence it may become a function of both incident energy and angle of incidence. In Fig. 21 values of Y^* are plotted against $E^{1/2}$ for various angles of incidence for H⁺-Ni. In the region of $\alpha < 60^\circ$ the linearity of Y^* is very good, while at $\alpha = 80^\circ$ Y^* is no longer linear. Then, the threshold energy of grazing angles of incidence will include a large ambiguity due to the bad linearity so long as we use Eq. (31) in determining the threshold energy at grazing angles of incidence.

The bombarding-angle dependences of threshold energies of $\text{Hg}^+\text{-Ni}$, $\text{Ar}^+\text{-Cu}$, and $\text{H}^+\text{-Ni}$ are shown in Fig. 22. The solid lines are the present results, and the vertical error bars mean the ambiguities due to the poor linearity of Y^* versus $E^{1/2}$. In the case of light-ion sputtering the ACAT threshold energy is a slightly increasing function of angle of incidence α , while that of heavy-ion sputtering has the minimum value near $\alpha = 60^\circ$. The strong α -dependence of the near-threshold sputtering of heavy ions in the region of $\alpha < 60^\circ$ can be explained by the fact that the threshold energy of heavy-ion sputtering is a decreasing function of α until 60° .

A few-collision sequence model²⁷ indicates that the threshold energy for small angles of incidence is given as

$$E_{\text{th}} = \begin{cases} \frac{U_s}{\gamma} \frac{1}{\sin^{12} \left(\frac{2\pi + \alpha}{6} \right)} & M_1 > M_2 \\ \frac{U_s}{\gamma} \left(\frac{1 + \mu}{1 + \mu \cos[(\pi - \alpha)/3]} \right)^6 & M_1 < M_2 \end{cases} \quad (37)$$

which is obtained from Tables 5 and 6 if we use $m=2$ as the collision number. Equation (37) tells us some interesting bombarding-angle dependences of the threshold energies. In the case of $M_1 > M_2$ the threshold energy shows a universal dependence on bombarding-angle, which comes from the fact that the moving atom in solids is always a target atom. This means that the mass-ratio dependence is expressed only by $1/\gamma$. In the case of $M_1 < M_2$ the α -dependence is more complicated and depends also on the mass-ratio. For light ions, however, the threshold energy has only a weak dependence of α .

When the angle of incidence becomes larger we should take into account the shadowing effect and the periodicity of surface atoms²⁷. In Fig. 23 the relative threshold energies of different mechanisms are plotted as a function of angle of incidence for $\text{Hg}+\text{Ni}$, $\text{Ar}+\text{Cu}$, and $\text{H}+\text{Ni}$ combinations. Each dash line means the analytical formula of Eq. (37), and the solid lines with different marks indicate the numerical solutions when the shadowing effect and the periodicity of the nearest neighbor surface atoms are taken into account. For different mechanisms the data are calculated until the total reflection occurs. In the case of $\text{Hg}+\text{Ni}$ combination, the threshold mechanism is Mechanism 1D for small angles of incidence, and Mechanism 2B becomes the threshold mechanism for grazing angles of incidence. Another interesting aspect of the α -dependence of $\text{Hg}+\text{Ni}$ is that the threshold energy is a decreasing function of α until 60° . This tendency is exactly coincident with that of the ACAT threshold energy. In the case of medium-ion sputtering such as $\text{Ar}+\text{Cu}$ combination the α -dependence of threshold energy is more complicated than other two cases. For small angles of incidence the threshold mechanism is Mechanism 2C, and around $\alpha \approx 55^\circ$ the threshold mechanism is

Mechanism 1D. For grazing angles of incidence Mechanism 2B becomes the threshold mechanism. The bombarding-angle dependence of light-ion sputtering thresholds is much different from medium-ion and heavy-ion sputtering thresholds. Threshold energies of Mechanisms 2A, 2B, and 2C have the almost same values until 80° , but for larger angles of incidence than 80° the threshold mechanism is Mechanism 2B. The real threshold energy of light-ion sputtering is nearly constant until 85° .

From Fig. 23 we can derive a common feature. For small angles of incidence many collision process is the threshold mechanism, while for larger angles of incidence the simpler mechanism becomes important. In the case of heavy-ion sputtering the threshold mechanism at small angle of incidence is Mechanism 1D whose threshold energy is a decreasing function of angle of incidence, while that of light-ion sputtering is Mechanism 2C whose threshold energy is nearly constant. The threshold mechanism of medium-ion sputtering depends strongly on angle of incidence, because the energy transfer at a single collision is relatively large as compared with light-ion collision.

3.5 Angular distribution of sputtered atoms at oblique incidence

Using the ACAT program, we calculated the angular distributions of sputtered atoms at oblique incidence, where we chose $\text{Hg}^+ - \text{Ni}$, $\text{Ar}^+ - \text{Cu}$, and $\text{H}^+ - \text{Ni}$ as the ion-target combinations. In order to reduce the statistical error we used large acceptance solid angle, i.e., $\Delta\beta = 10^\circ$ and $\Delta\phi = 40^\circ$, where $\Delta\beta$ and $\Delta\phi$ are the intervals of polar angle and azimuthal angle of sputtered atoms, respectively. This acceptance solid angle is too large for grazing angle of incidence, especially for light-ion sputtering.

In Fig. 24 we show the angular distributions of sputtered atoms for 1000eV $\text{Hg} \rightarrow \text{Ni}$. The preferential angle of ejection depends on the angle of incidence. Figure 25 shows the angular distributions for 100eV $\text{Hg} \rightarrow \text{Ni}$. It is very interesting that the preferential angle does not depend on angle of incidence. This is mainly due to the fact that the preferential angle of sputtered atoms for near-threshold sputtering is determined by surface scattering.

In Figs. 26, 27, and 28 we show the angular distributions of sputtered atoms for 100eV Ar ions, 100eV Ar ions, and 50eV Ar ions, respectively, which are bombarded on copper target with different angles of incidence. In the case of 1000eV ions, the argon ions can penetrate deeply into the solid for $\alpha = 40^\circ$ and $\alpha = 60^\circ$, and so the backward component of angular distribution is nearly equal to that of normal incidence. In the case of 50eV ions the preferential angle does not depend on the angle of incidence. This characteristic aspect is similar to the case of 100eV $\text{Hg}^+ \rightarrow \text{Ni}$.

In Figs. 29 and 30 we compare the ACAT angular distributions with the TRIM results and the measured distributions^{28,29}. As is known from the measured angular distributions

the angular distributions of light-ion sputtering at oblique incidence are composed of two parts, i.e., one due to the direct knock-off process at the topmost layer³⁰ by the incoming ions and the other due to the collision cascade by ions reflected from the deep layer in solids. The former part has the explicit preferential angle of sputtered atoms, while the latter part makes broad peak near the surface normal. The ACAT distributions include the contribution from the second component, but its contribution is not so clear as compared with the measured distributions due to too-large acceptance solid angle.

In order to know the contribution of the collision cascade generated by backscattered ions more clearly we follow the reflected position x_p of the ion which returns back to the surface and generates the recoil atom leading to sputtering. In Fig. 31 we show the x_p -dependence of the angular distributions of sputtered atoms for 450eV H^+ \rightarrow Ni, where the angle of incidence is 70° . The blank area means the angular distribution due to the knock-off process, i.e., $x_p < 5\text{\AA}$. The mesh area means the contribution of recoil atoms due to the ion which is reflected in region $5\text{\AA} < x_p < 10\text{\AA}$. The hatched area means that of recoil atoms produced by the ions which reflected in the deeper layer than 10\AA . From this figure we know clearly that the angular distributions of light-ion sputtering at oblique incidence are composed of two parts which is already described above.

IV Conclusion

Using the Monte Carlo program ACAT, the incident energy dependence and the bombarding angle dependence of low-energy sputtering have been investigated. Using the ACAT results of low-energy sputtering yields, we derive the mass-ratio dependence of sputtering thresholds with the help of the empirical Matsunami formula and compare the ACAT threshold energy with the recent theoretical result. And it is found that the agreement between two approaches is very good.

As for the oblique incidence of low-energy ions we found that the bombarding-angle dependence of the low-energy heavy-ion sputtering is very strong and the finite number of sputtered atoms can be observed near $\alpha = 60^\circ$ even if the incident energy is less than the threshold energy at normal incidence. It is found that this strong α -dependence can be explained by the fact that the threshold energy of heavy-ion sputtering is a decreasing function of α until 60° .

The angular distributions of sputtered atoms are also calculated using the ACAT program. It is found that the angular distributions of low-energy sputtering have much different profiles from those predicted by the linear-collision-cascade theory¹.

References

- 1) P. Sigmund, Phys. Rev. 184 (1969) 383.
- 2) J.P. Biersack and L.G. Haffmark, Nucl. Instr. Methods 174 (1980).
- 3) W. Takeuchi and Y. Yamamura, Rad. Eff. 71 (1983) 53.
- 4) T. Ishitani and R. Shimizu, Jpn. J. Appl. Phys. 11 (1972) 125.
- 5) D.E. Harrison, W.L. Moore, and H.T. Holcombe, Rad. Eff. 17 (1973) 167.
- 6) M.I. Baskes, J. Nucl. Mater. 128&129 (1984) 676.
- 7) M.T. Robinson and I.M. Torrens, Phys. Rev. B9 (1974) 5008.
- 8) J.P. Biersack and W. Eckstein, Appl. Phys. A34 (1984) 73.
- 9) N. Matsunami, Y. Yamamura, Y. Itikawa, N. Itoh, Y. Kazumata, S. Miyagawa, K. Morita, R. Shimizu, and H. Tawara, ATOMIC DATA AND NUCLEAR DATA TABLES 31 (1984) 1.
- 10) E. Everhart, G. Stone, and R.J. Carbone, Phys. Rev. 99 (1955) 1287.
- 11) G. Moliere, Z. Naturforsch. 2A (1947) 133.
- 12) W.D. Wilson and C.L. Bisson, Phys. Rev. B3 (1971) 3984.
- 13) J.P. Ziegler, J.P. Biersack, and U. Littmark, Proc. IPAT'83, Kyoto (1983) p1861.
- 14) P. Gombas, Encyclopedia of Physics, vol. XXXVI, 109 Berlin, Springer (1956).
- 15) P. Loftager, F. Besenbacher, O.S. Jensen, and V.S. Sorensen, Phys. Rev. A20 (1979) 1443.
- 16) N. Nakagawa, S. Enoki, and Y. Yamamura, to be published.
- 17) H.H. Andersen and J.F. Ziegler, "The Stopping and Ranges of Ions in Matter" vol. 3 Pergamon Press (1977) and J.F. Ziegler, vol. 4 (1977).
- 18) C. Varelas and J.P. Biersack, Nucl. Instr. Methods 79 (1970) 213.
- 19) J. Lindhard, M. Scharff, and H.E. Schiøtt, K. Dan. Vidensk. Selsk. Mat.-Pys. Medd. 33, no. 14 (1963).
- 20) O.S. Oen and M.T. Robinson, Nucl. Instr. Methods 132 (1976) 647.
- 21) M.W. Weissmann and R. Behrisch, Rad. Eff. 19 (1973) 69.
- 22) Y. Yamamura, N. Matsunami, and N. Itoh, Rad. Eff. 71 (1983) 65.
- 23) J. Bohdansky, Nucl. Instr. Methods 2B (1984) 587.
- 24) D.E. Harrison and G.D. Magnuson, Phys. Rev. 122 (1961) 1421.
- 25) R. Behrisch, G. Maderlechner, B.M.U. Scherzer, and M.T. Robinson, Appl. Phys. 18 (1981) 391.
- 26) Y. Yamamura and Y. Mizuno, J. Nucl. Mater. 128&129 (1984) 559.
- 27) Y. Yamamura and J. Bohdansky, to be published
- 28) J. Roth, J. Bohdansky, and W. Ottenberger, IPP 9/26, Max-Planck-Institut für Plasmaphysik (1979)
- 29) J. Bohdansky, "DATA COMPENDIUM FOR PLASMA-SURFACE INTERACTIONS" edited by R.A. Langley, IAEA, Vienna (1984) p61.
- 30) Y. Yamamura, Nucl. Instr. Methods B2 (1984) 578.

Table 1 Various screening functions available in the ACAT program

Screening function		Screening length
Thomas-Fermi (Sommerfeld)	$[1 + (x/12^{2/3})^k]^{3/k}$ (k = 0.8034)	
Moliere	$0.35e^{-0.3x} + 0.55e^{-1.2x} + 0.10e^{-6.0x}$	$\frac{0.4685}{(z_1^{1/2} + z_2^{1/2})^{2/3}}$
Kr-C	$0.190945e^{-0.131825x} + 0.473674e^{-0.63717x}$ $+ 0.335381e^{-1.919249x}$	
Ziegler	$0.18175e^{-3.1998x} + 0.50986e^{-0.94229x}$ $+ 0.28022e^{-0.4029x} + 0.028171e^{-0.20162x}$	$\frac{0.4685}{z_1^{0.23} + z_2^{0.23}}$
Lenz-Jensen # (LJ)	$e^{-3.11y}(1 + 3.11y + 3.24y^2 + 1.46y^3$ $+ 0.248y^4)$	
aLJ §	$e^{-t}(1 + 0.9839t + 0.4272t^2$ $+ 0.01150t^3 + 0.01288t^4)$	
aMLJ	$\exp(-A_{12}x + B_{12}x^{3/2} - C_{12}x^2)$ $A_{12} = 1.694[G(0.4092)/G(2/3)]^{1/2}$ $B_{12} = 0.7629G(0.1687)/G(2/3)^{3/4}$ $C_{12} = 0.1206G(0.2789)^2/G(2/3)$ $G(m) = z_1^m + z_2^m$	$\frac{0.4685}{(z_1^{2/3} + z_2^{2/3})^{1/2}}$

: $y = \sqrt{x}$

§ : $t = \sqrt{9.67x}$

Table 2 The screening lengths and the surface binding energies used in the present calculations

Ion-target combination	Mass ratio M_2/M_1	Surface binding energy U_s (eV)	Screening length a (Å)
H + Ni	58.2	4.44	0.1375
He + Ni	14.7	4.44	0.1054
Ne + Pt	9.67	5.85	0.07153
Ar + Au	4.93	3.81	0.08417
Ar + Ag	2.70	2.95	0.09416
Ar + Cu	1.59	3.49	0.1035
Ni + Ni	1.00	4.44	0.06804
Hg + Ni	0.293	4.44	0.07976
Hg + Al	0.135	3.39	0.08675
Hg + C	0.0599	7.37	0.09253

Table 3 The ACAT results of sputtering yields at normal incidence for various ion-target combinations

Ion	Target	Energy (eV)	Y_I	Y_{II}	Y_{tot}	Y_p	N_0
H	Ni	100	—	—	0.00039	0.00034	80000
		200	0.00020	0.00608	0.00628	0.00442	50000
		1000	0.00116	0.0151	0.0163	0.00708	25000
He	Ni	30	—	—	0.00064	0.00063	200000
		100	0.0033	0.0506	0.0539	0.0329	30000
		1000	0.0520	0.121	0.173	0.0368	10000
Ne	Pt	30	—	—	0.00076	0.00074	50000
		100	0.0109	0.0859	0.0968	0.0666	10000
		1000	0.533	0.401	0.933	0.180	1000
Ar	Au	20	—	—	0.00789	0.00750	50000
		100	—	—	0.472	0.289	1000
		1000	2.68	1.05	3.73	0.628	500
Ar	Ag	15	—	—	0.00200	0.00198	150000
		100	—	—	0.516	0.213	4000
		1000	3.61	0.525	4.14	0.421	500
Ar	Cu	20	—	—	0.00067	0.00044	500000
		100	—	—	0.345	0.136	10000
		1000	3.10	0.124	3.22	0.321	3000
Ni	Ni	30	—	—	0.00042	0.00012	50000
		100	0.0866	0.00020	0.0868	0.0101	10000
		1000	1.65	0.0572	1.71	0.122	1000
Hg	Ni	40	—	—	0.00002	0.0	200000
		100	0.0304	0.00012	0.0305	0.00141	50000
		1000	1.97	0.0114	1.98	0.0909	2000
Hg	Al	70	—	—	0.00372	0.00076	50000
		200	0.128	0.00076	0.129	0.0128	4000
		1000	0.953	0.00210	0.955	0.0785	500
Hg	C	300	—	—	0.00083	0.00006	50000
		1000	0.112	0.00020	0.112	0.0104	5000
		10000	0.960	0.0	0.960	0.130	100

Table 4 Threshold energies determined from the Matsunami empirical formula using the ACAT data

Ion-target combination	Mass ratio M_2/M_1	E_{th}		E_{th}/U_s	
		$n = 2$	$n = 2.8$	$n = 2$	$n = 2.8$
H + Ni	58.2	85.8 ~ 86.4	67.3 ~ 70.8	19.3 ~ 19.5	15.2 ~ 16.0
He + Ni	14.7	25.9 ~ 26.4	20.6 ~ 23.3	5.8 ~ 6.0	4.6 ~ 5.3
Ne + Pt	6.61	25.6 ~ 27.9	21.5 ~ 22.4	4.4 ~ 4.8	3.7 ~ 3.8
Ar + Au	4.93	11.5 ~ 14.6	10.5 ~ 12.1	3.0 ~ 3.8	2.8 ~ 3.2
Ar + Ag	2.70	13.0 ~ 17.1	10.8 ~ 13.1	4.4 ~ 5.8	3.7 ~ 4.4
Ar + Cu	1.59	18.8 ~ 21.1	16.0 ~ 17.7	5.4 ~ 6.1	4.6 ~ 5.1
Ni + Ni	1.0	29.4 ~ 31.2	25.6 ~ 26.1	6.6 ~ 7.0	5.8 ~ 5.9
Hg + Ni	0.293	40.2 ~ 48.1	37.8 ~ 42.1	9.1 ~ 10.8	8.5 ~ 9.5
Hg + Al	0.135	53.4 ~ 59.8	40.6 ~ 49.9	15.8 ~ 17.6	12.0 ~ 14.7
Hg + C	0.0599	269.2 ~ 314.8	235.5 ~ 254.0	36.5 ~ 42.7	32.0 ~ 34.6

TABLE 5 Analytic formulae for threshold energy of each mechanism

MECHANISM	E_{th}	
1A	$\frac{U_s}{\gamma}$	$\frac{1}{\sin^4\left(\frac{\alpha}{2}\right)}$
1B	$\frac{U_s}{\gamma}$	$\frac{1}{\sin^6\left(\frac{\pi + 2\alpha}{6}\right)}$
1C	$\frac{U_s}{\gamma}$	$\frac{1}{\sin^8\left(\frac{\pi + \alpha}{4}\right)}$
1D	$\frac{U_s}{\gamma}$	$\frac{1}{\sin^{2m+8}\left[\frac{(m+2)\pi + 2\alpha}{2m+8}\right]}$

TABLE 6 Analytic formulae for threshold energy of each mechanism

MECHANISM	E_{th}
2A	$\frac{U_s}{\gamma} \frac{(1+\mu)^2 (1+2\mu \cos \theta_1 + \mu^2)}{(1+\mu \cos \theta_1)^4}$ $\hat{\theta} + 2\hat{\theta} = \pi - \alpha$
2B	$\frac{U_s}{\gamma} \frac{(1+\mu)^2 (1+2\mu \cos \theta_1 + \mu^2)^2}{(1+\mu \cos \theta_1)^6}$ $\hat{\theta} + 3\hat{\theta} = \pi - \alpha$
2C	$\frac{U_s}{\gamma} \frac{(1+\mu)^{2m+2} (1+2\mu \cos \theta_1 + \mu^2)^{2-m}}{(1+\mu \cos \theta_1)^6}$ $(m+1)\hat{\theta} + 3\hat{\theta} = \pi - \alpha$

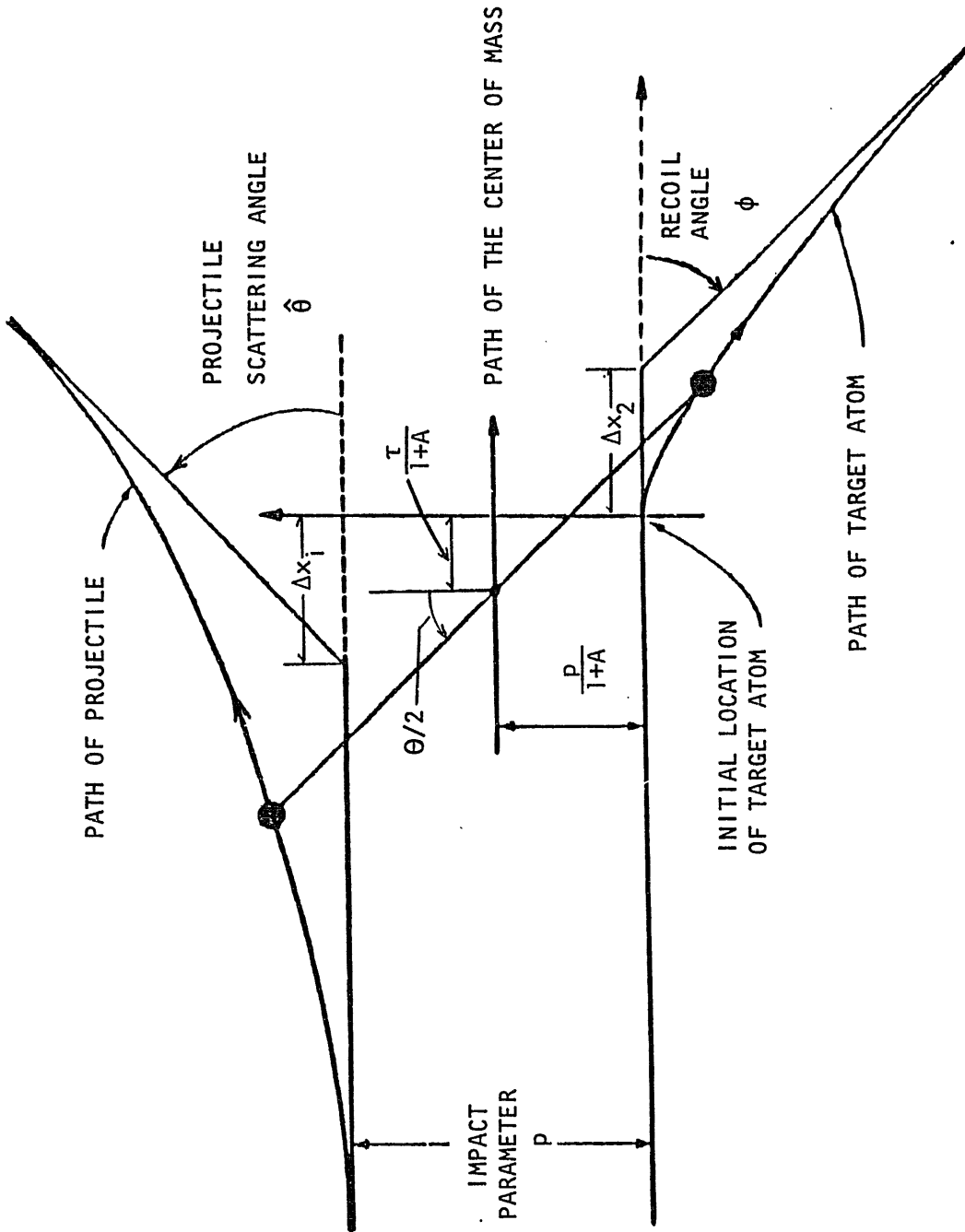


Fig. 1 The trajectories in the L system of two particles interacting according to the central repulsive force. The positions of the projectile and the target atom correspond to the apsis of the collision.

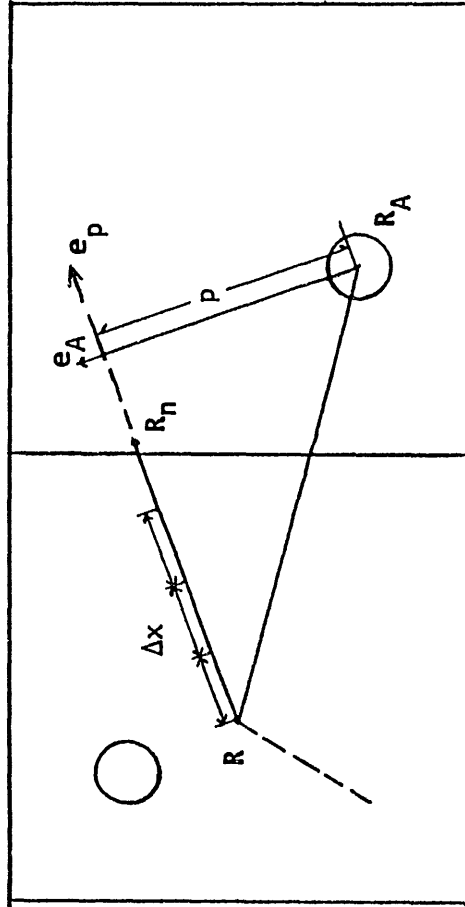


Fig. 2 Schematic representation of the procedure of searching a new collision partner inside the solid. e_p is a unit vector of the direction of a moving projectile, and R is the position vector of the initial location of the projectile. The interval Δx is usually equal to $R_0/5$.

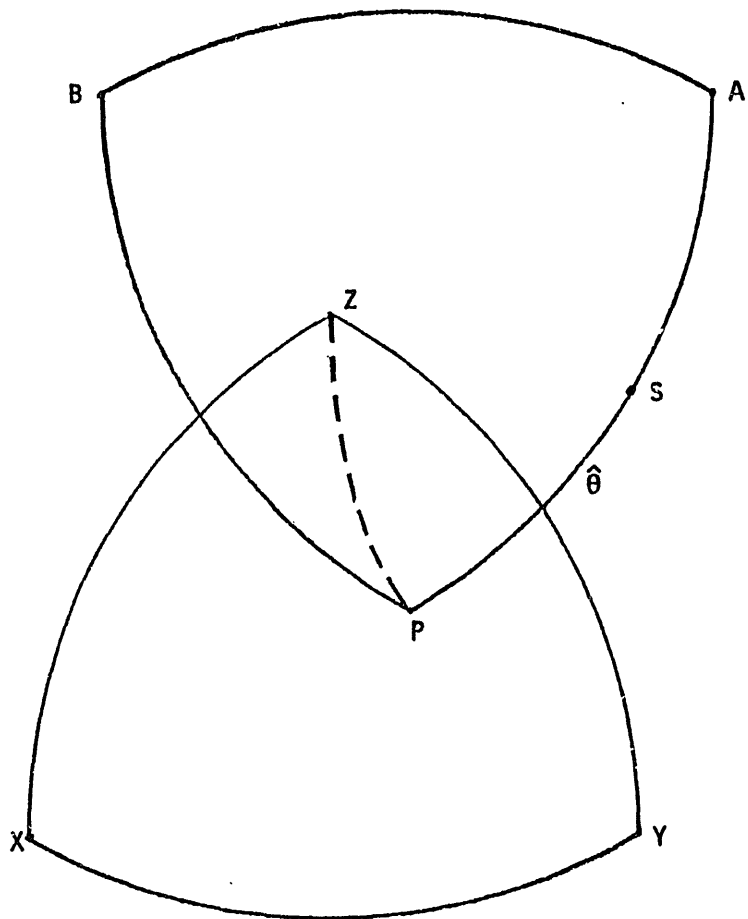


Fig. 3 Typical two coordinates in the spherical trigonometry, where X, Y, and Z are three axes of the absolute coordinate, and A, B, and P are those of the moving coordinate fixed to the projectile. The angle $\hat{\theta}$ is the scattering angle in the L system.

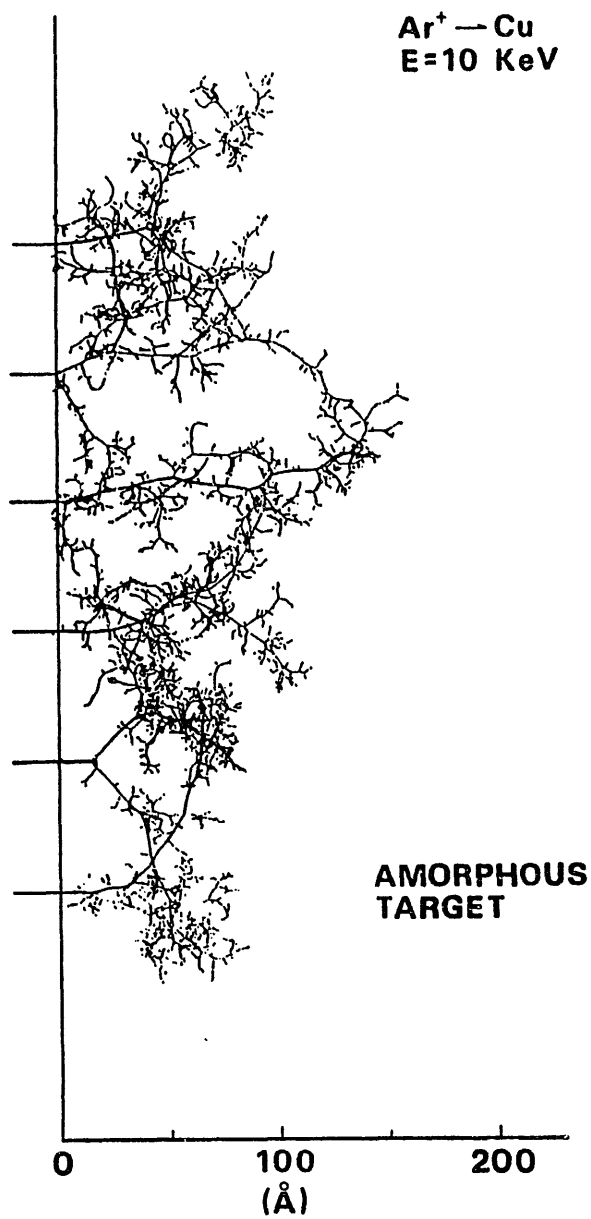


Fig. 5 Cascade developments in a copper target for 10 keV Ar → Cu, where the thin lines are the trajectories of recoil Cu atoms, and the broad lines are those of the Ar ions.

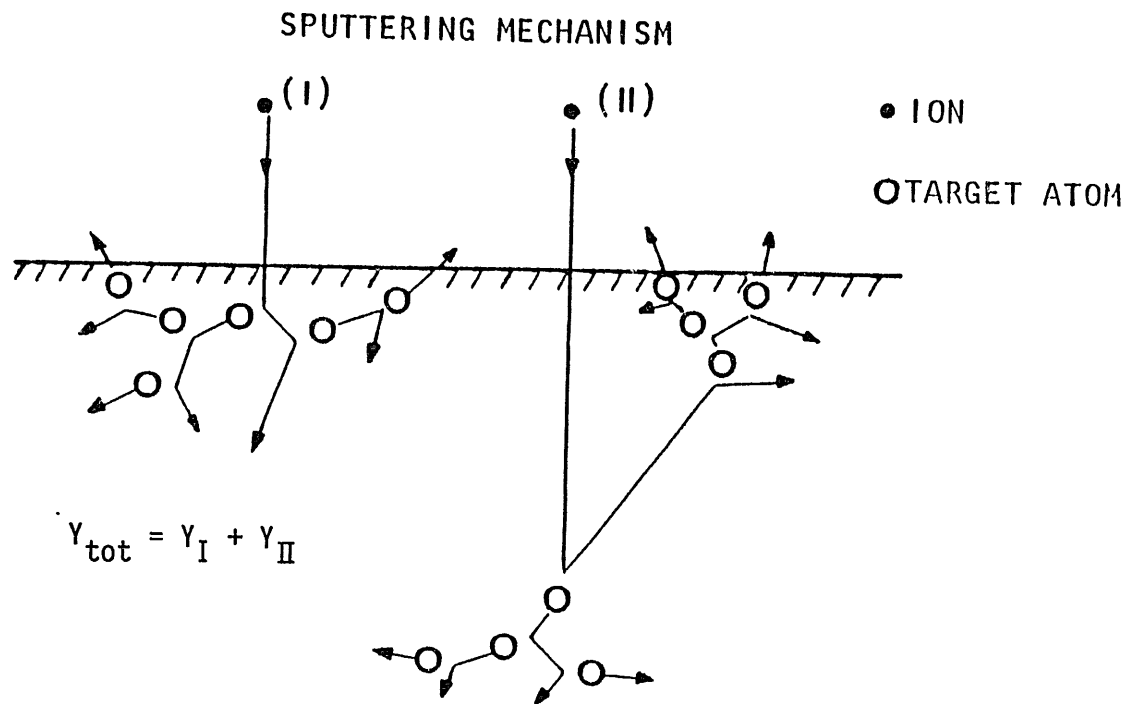


Fig. 6 Schematic representation of sputtering mechanisms

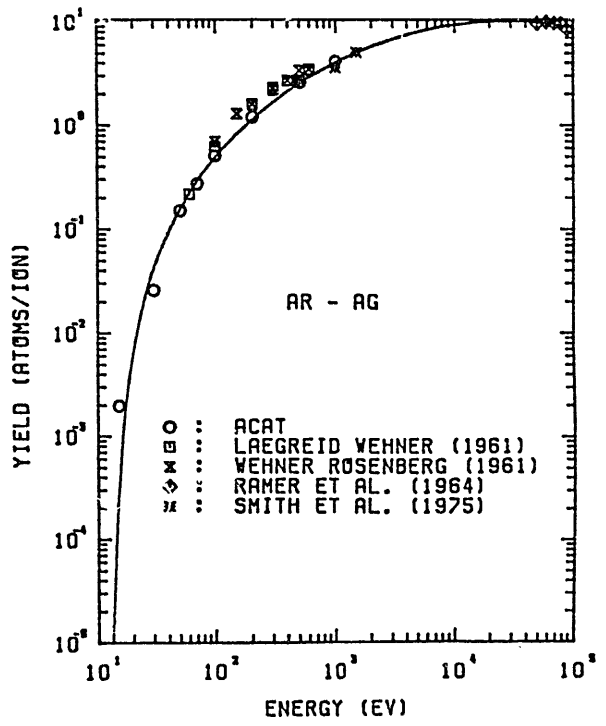
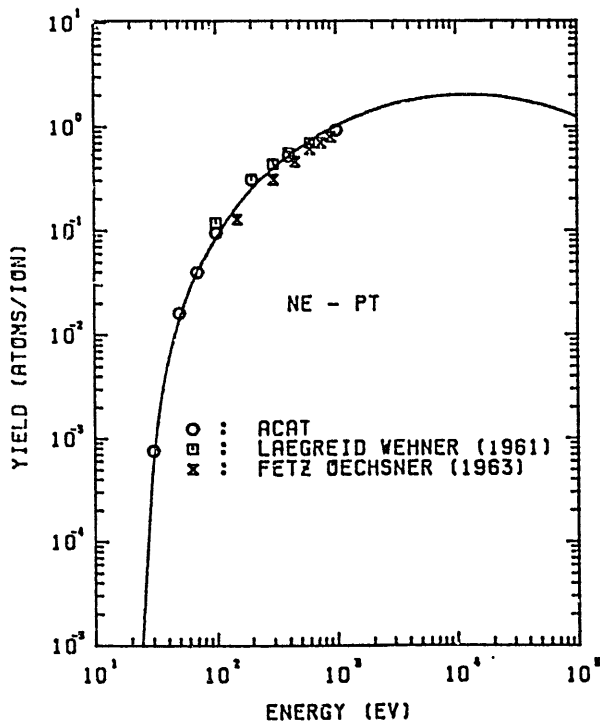
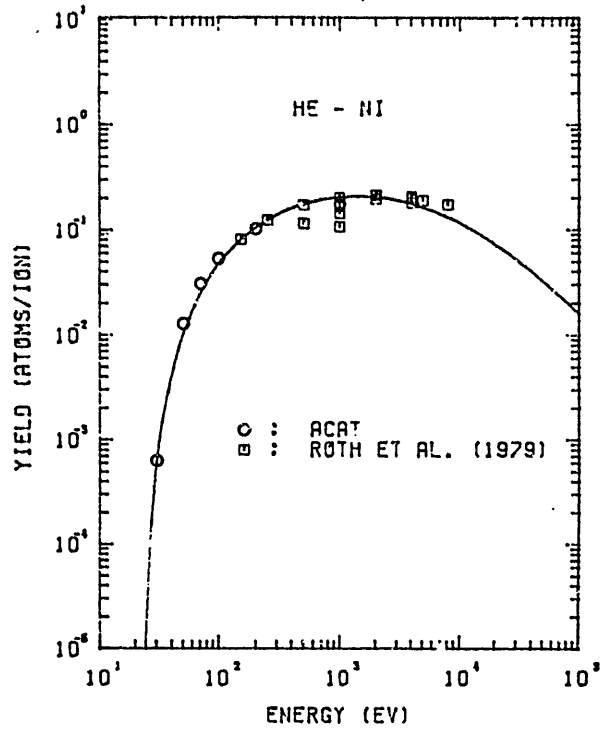
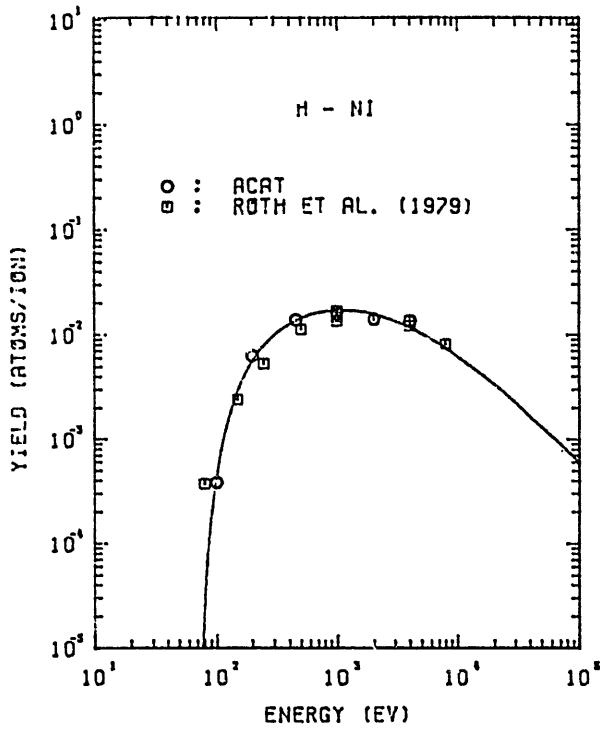


Fig. 7 The energy-dependences of sputtering yields at normal incidence for light-ion sputtering and medium-ion sputtering

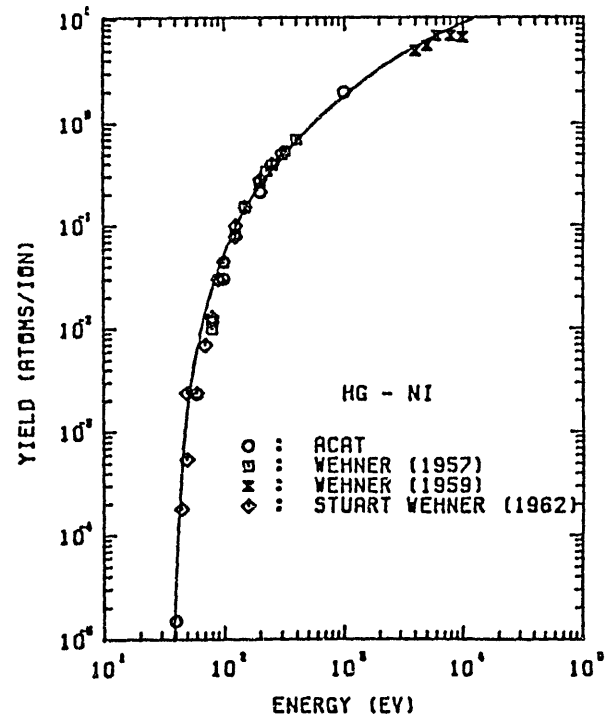
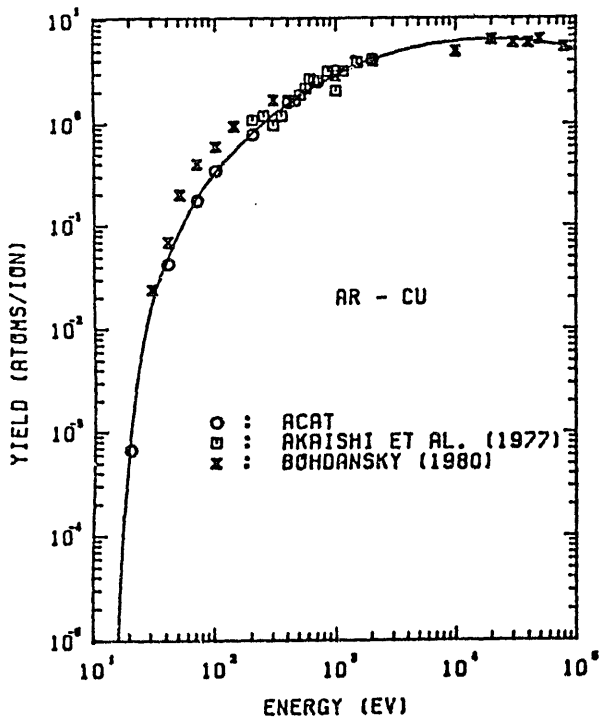
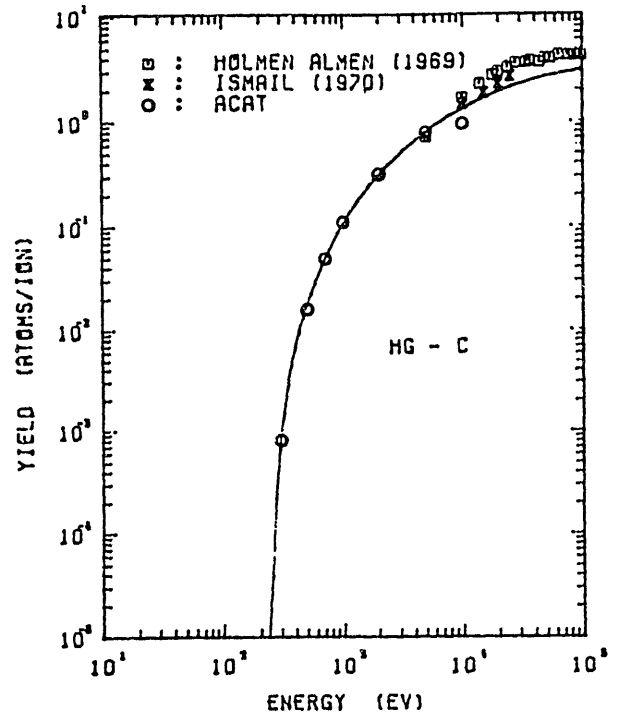
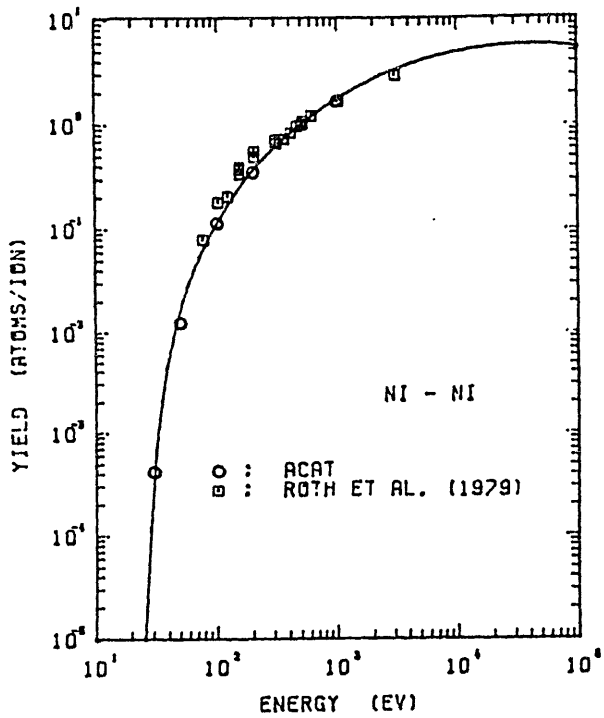


Fig. 8 The energy-dependences of sputtering yields at normal incidence for heavy-ion sputtering

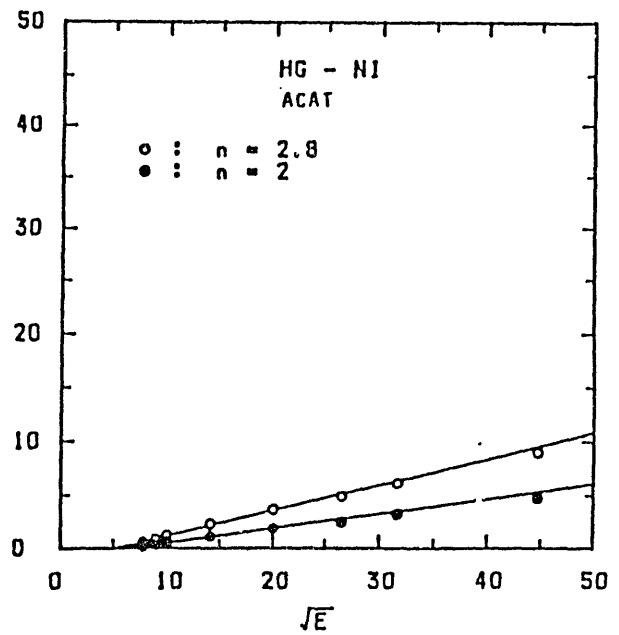
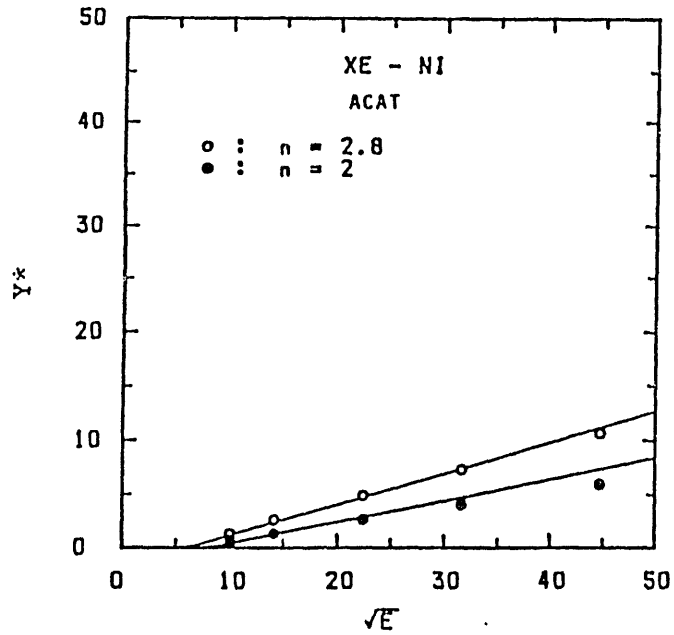
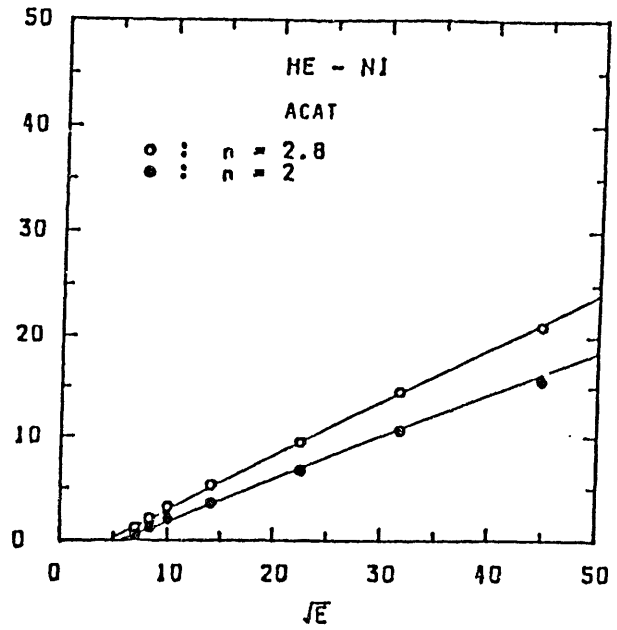
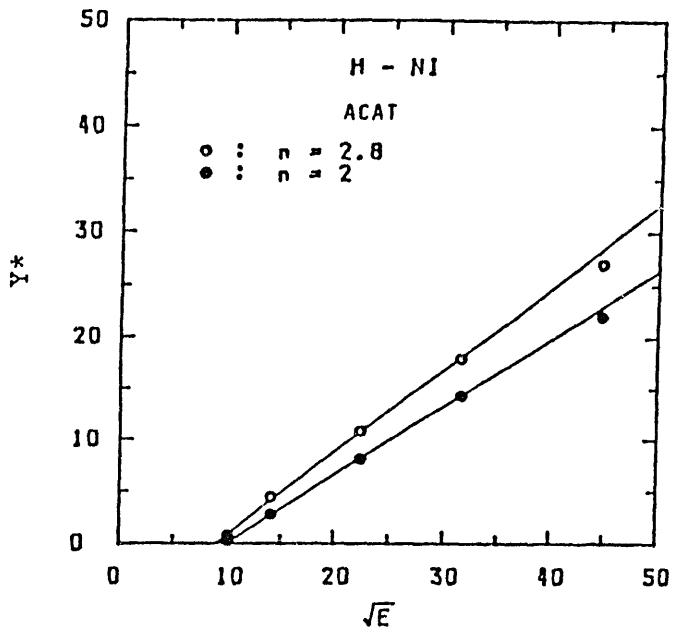


Fig. 9 Y^* of ACAT data plotted against $E^{1/2}$

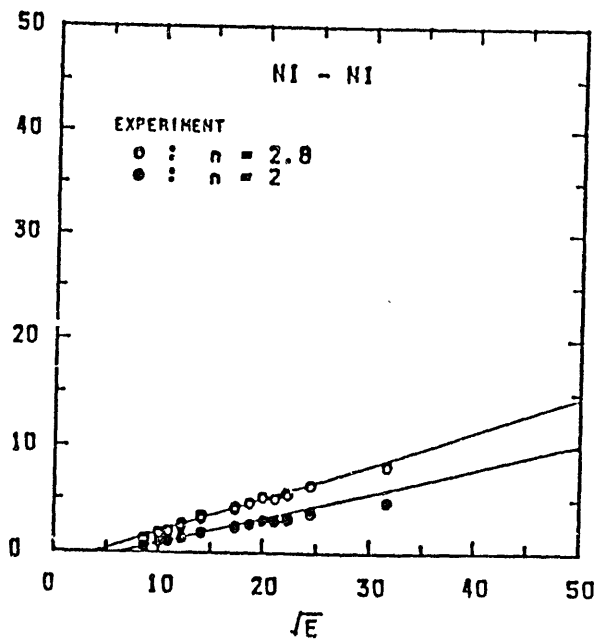
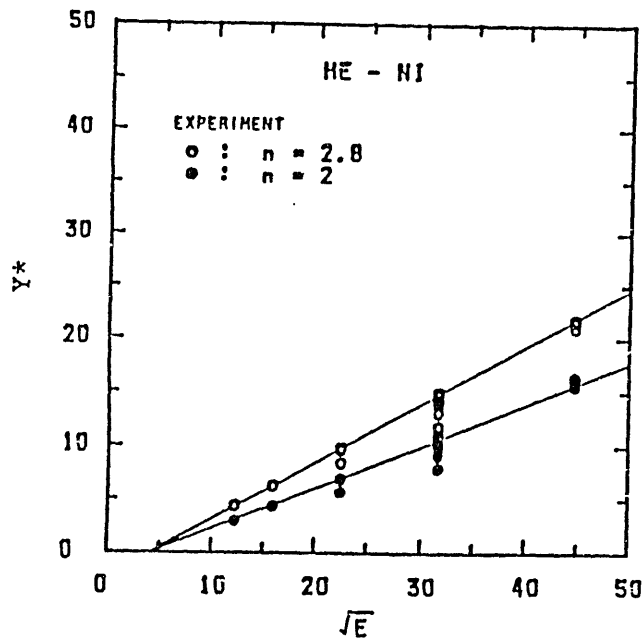
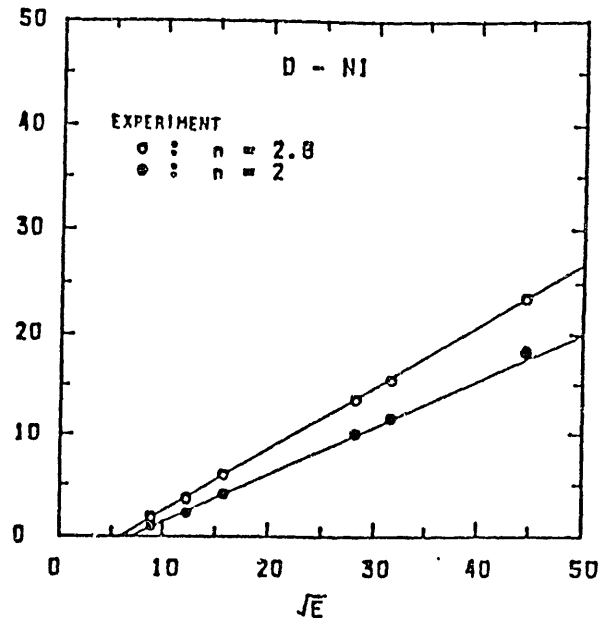
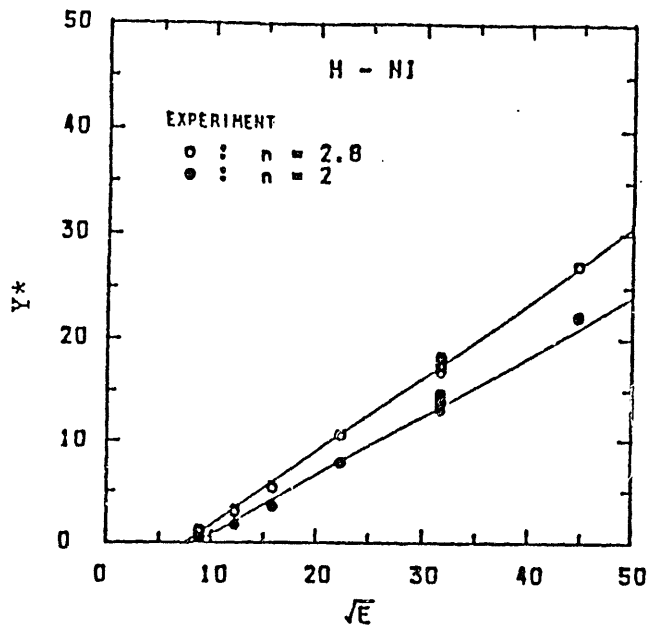


Fig. 10 Y^* of measured data plotted against $E^{1/2}$

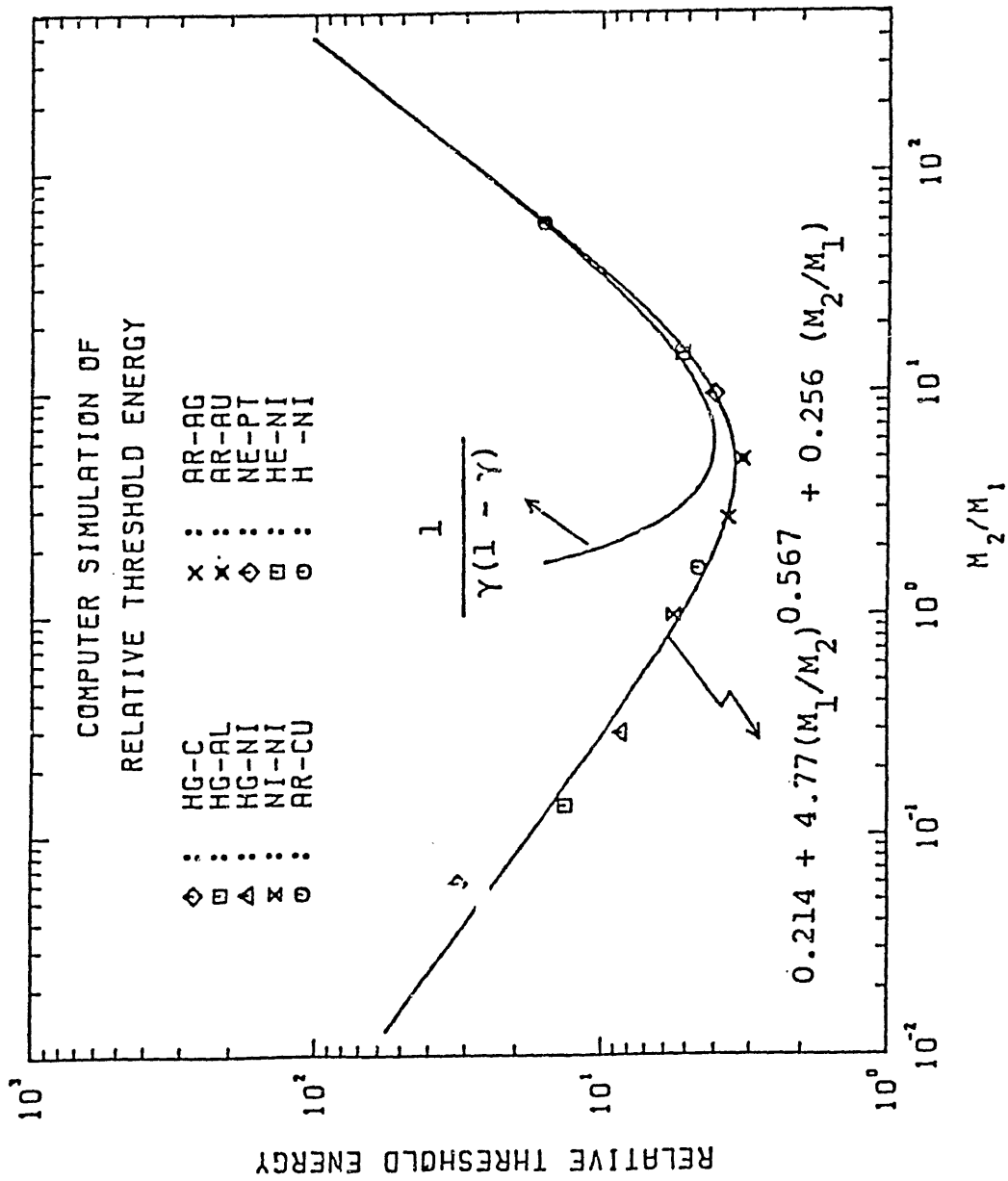


Fig. 11 The mass-ratio dependence of threshold energies which are determined from ACAT data.

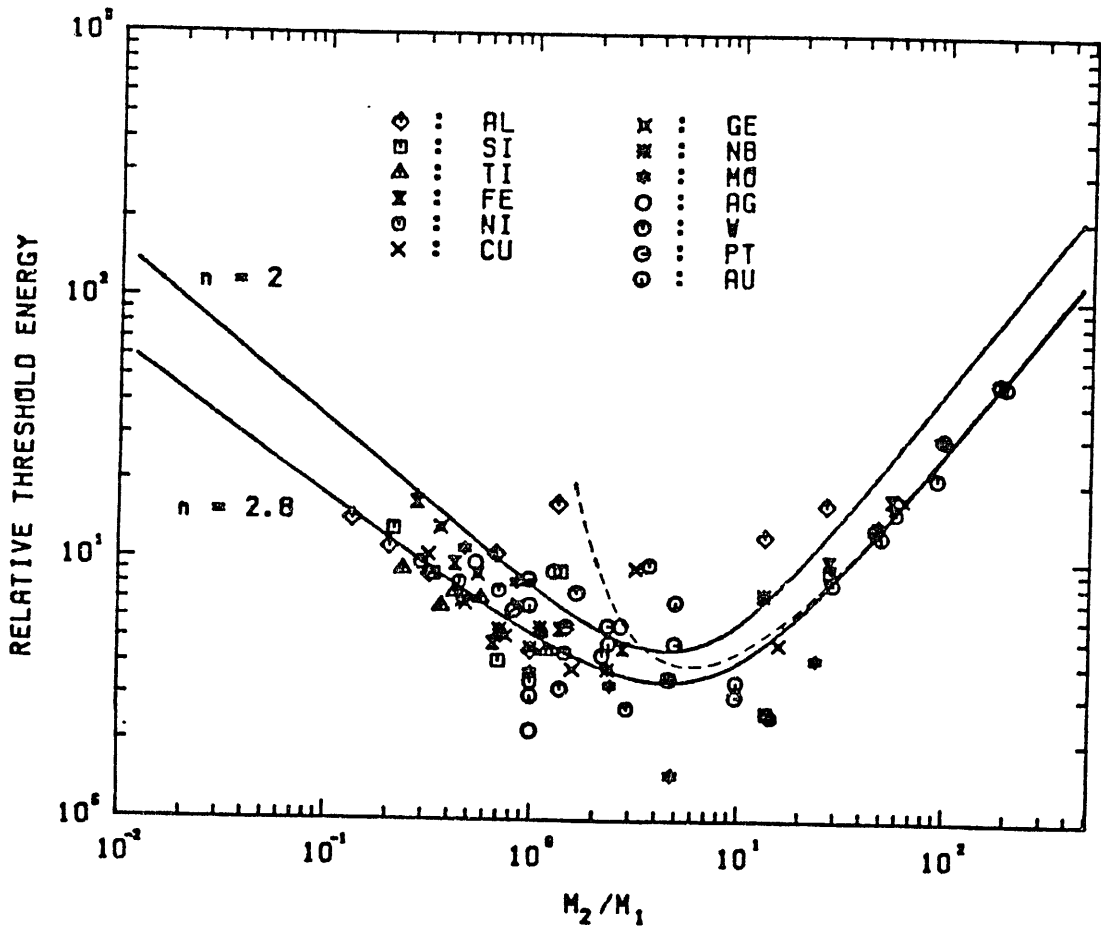
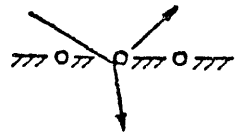


Fig. 12 Comparison between the ACAT threshold energy and experimental threshold energies which are determined from Eq. (31) using the various experimental data.

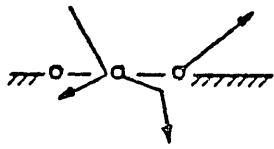
MECHANISM 1



MECHANISM 1A

1B'

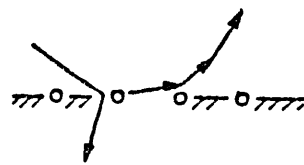
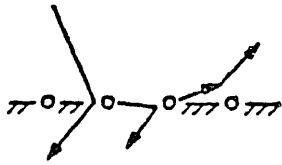
1B''



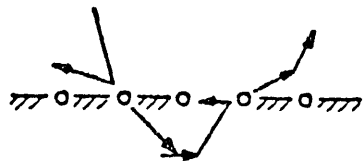
MECHANISM 1B

1C'

1C''



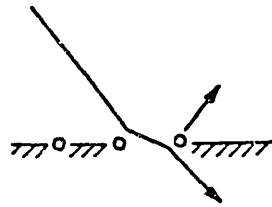
MECHANISM 1C



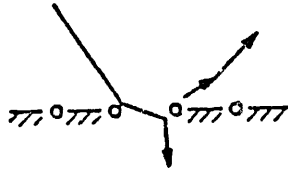
MECHANISM 1D

Fig. 13 Possible mechanisms for heavy-ion threshold sputtering

MECHANISM 2



MECHANISM 2A



MECHANISM 2B



MECHANISM 2C

Fig. 14 Possible mechanisms for light-ion threshold sputtering

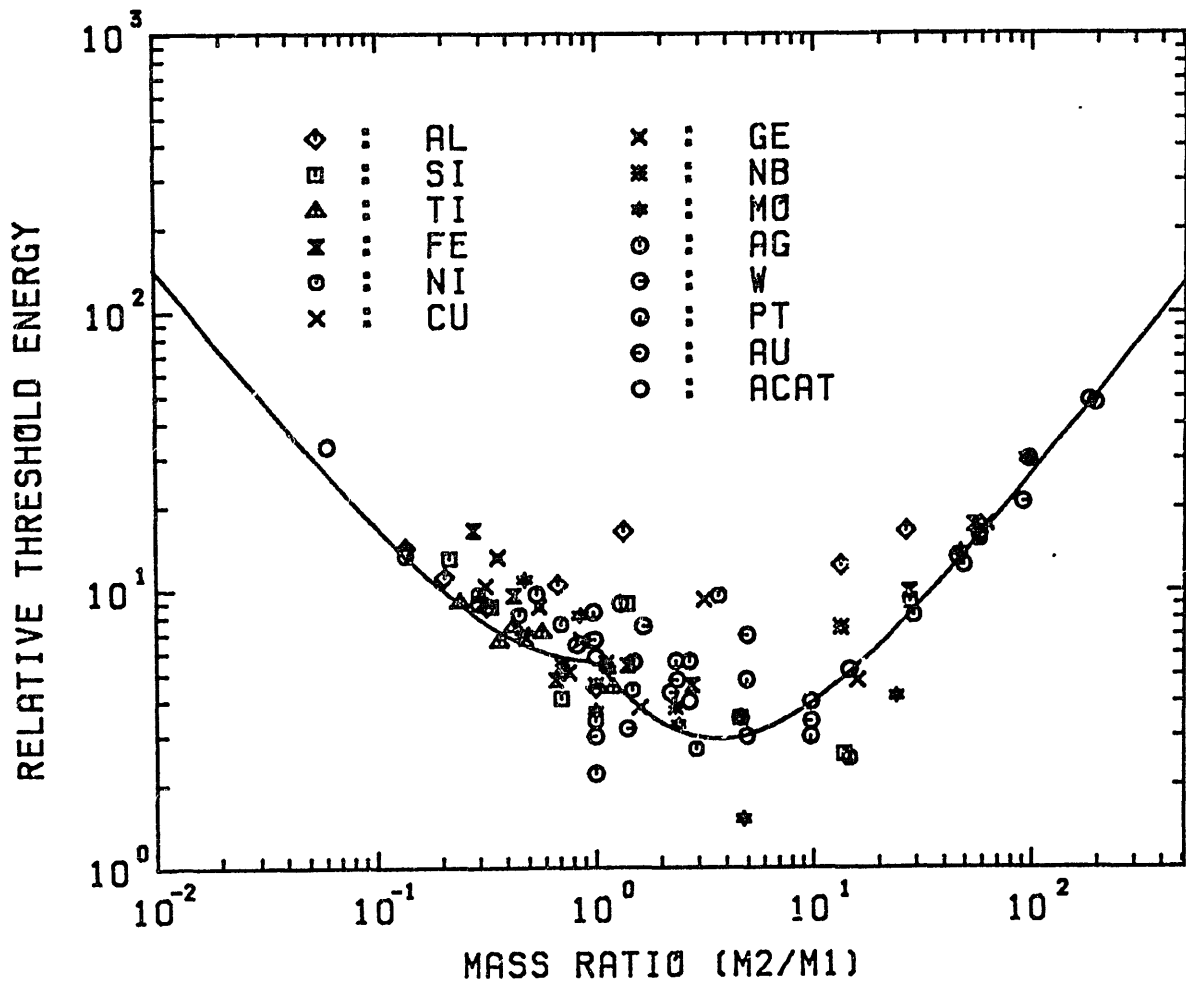


Fig. 15 Comparison between theoretical threshold energies and experimental ones. Theoretical values are calculated from Eq. (36) and experimental ones are those in Fig. 12.

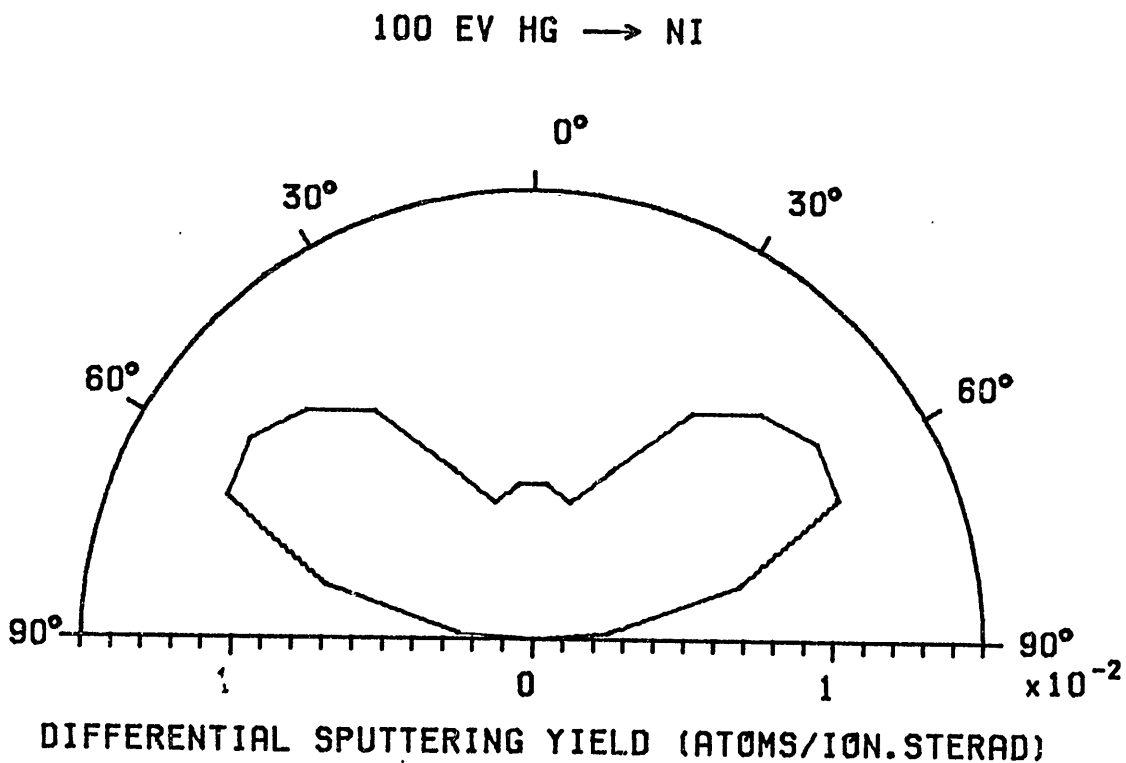
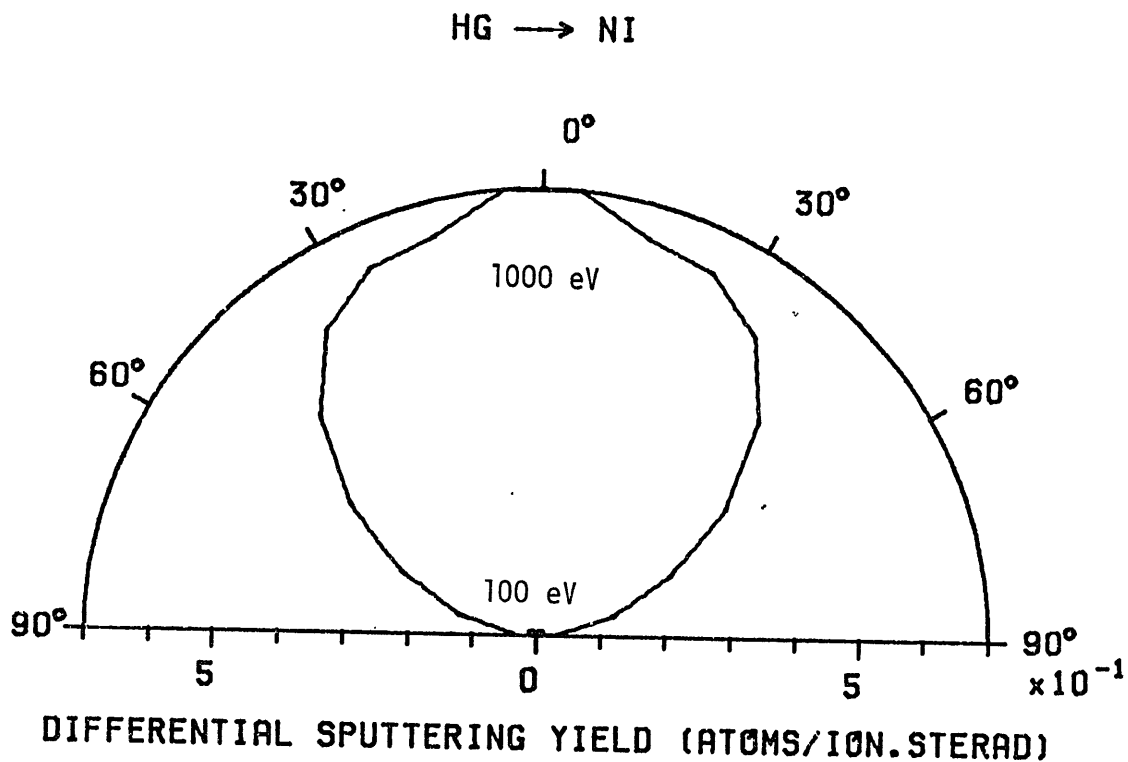


Fig. 16 Angular distributions of sputtered atoms for $\text{Hg}^+ \rightarrow \text{Ni}$ at normal incidence

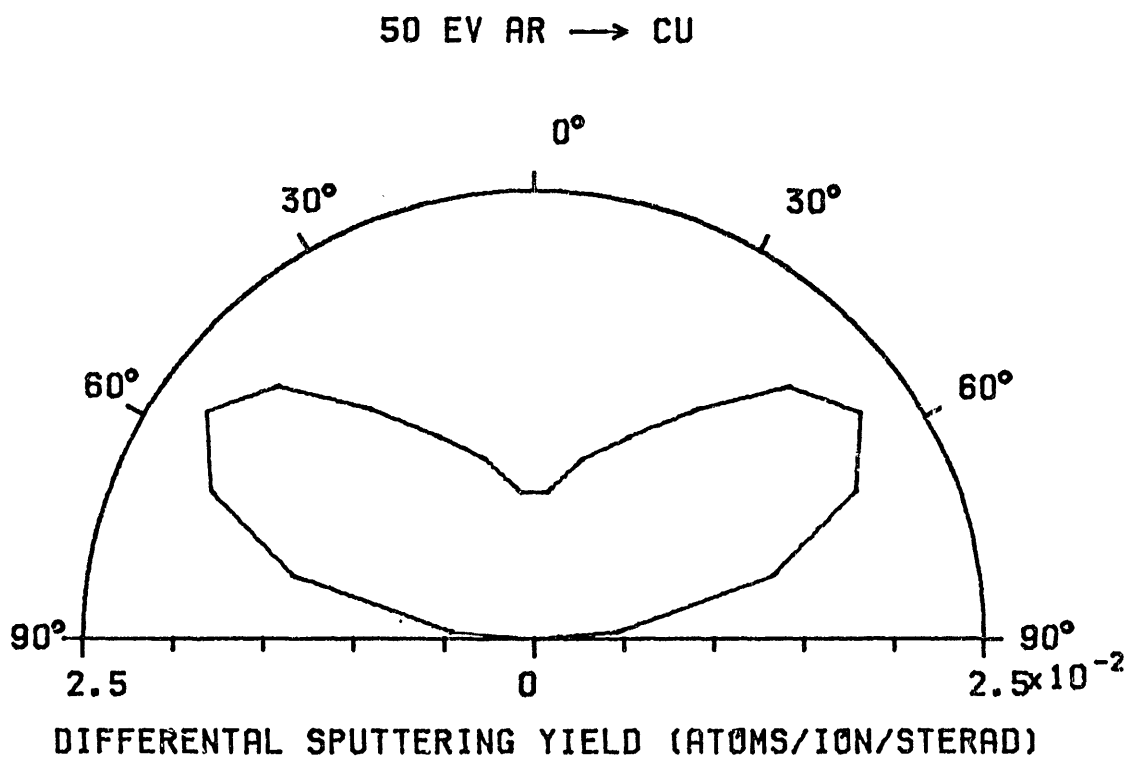
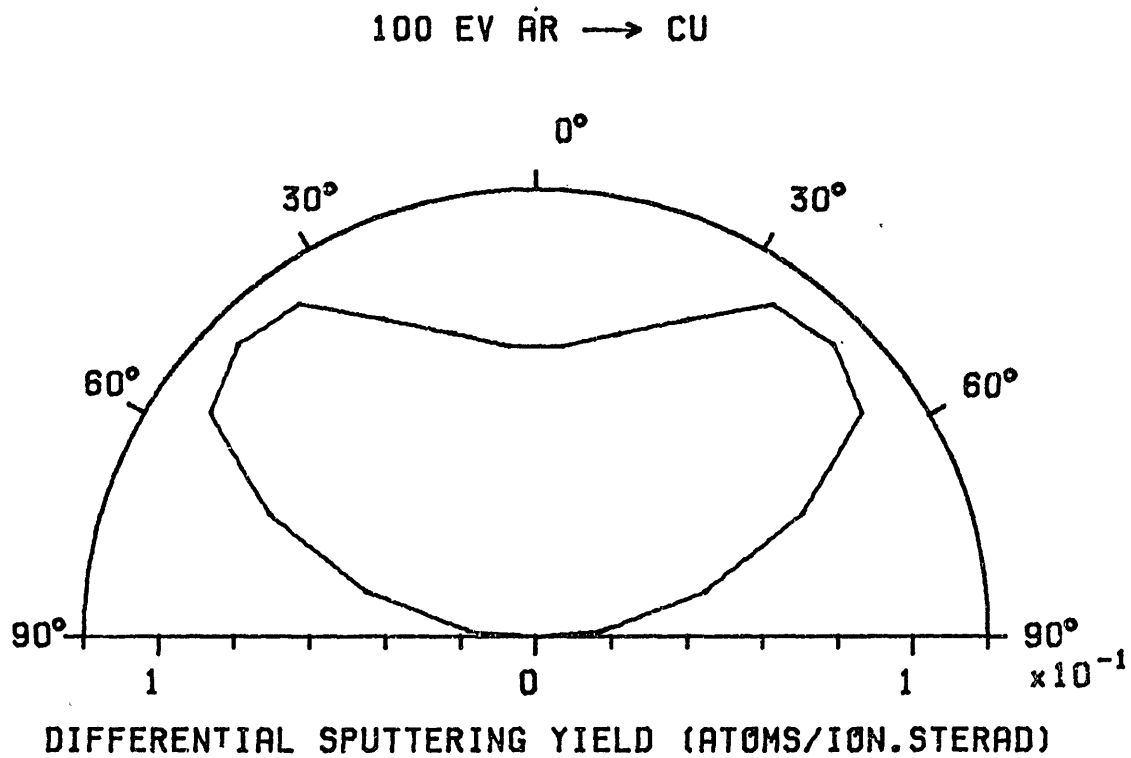


Fig. 17 Angular distributions of sputtered atoms for $\text{Ar}^+ \rightarrow \text{Cu}$ at normal incidence.

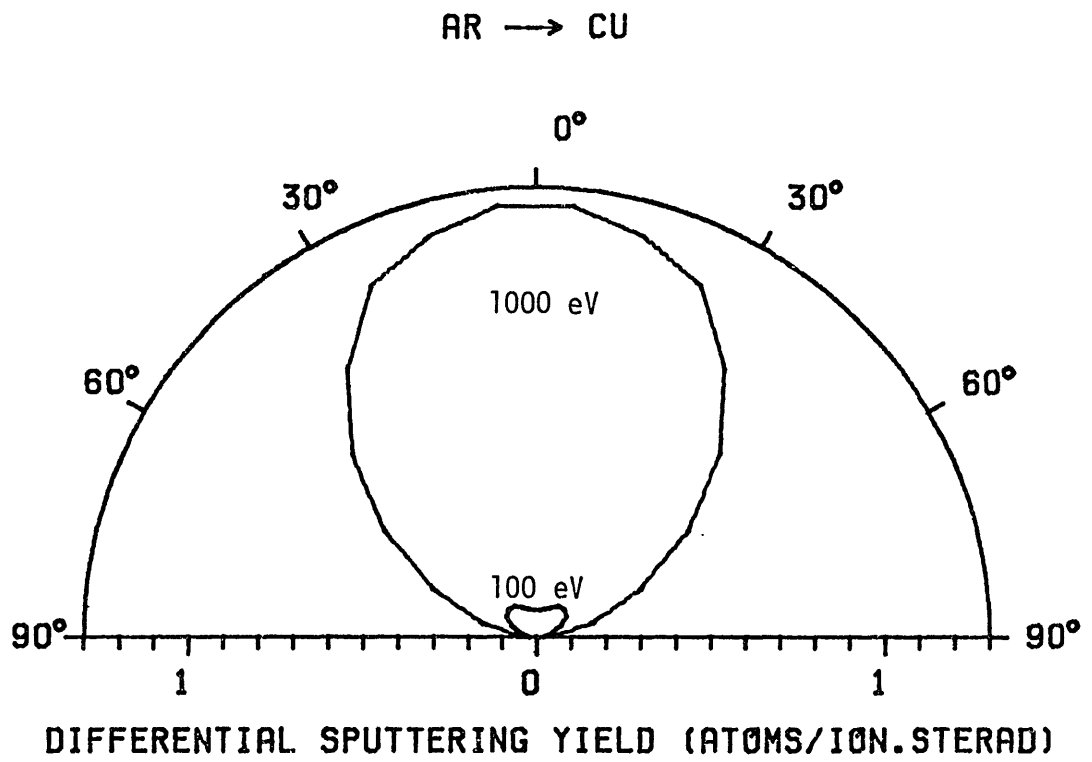


Fig. 18 Angular distributions of sputtered atoms for $\text{Ar}^+ \rightarrow \text{Cu}$ at normal incidence

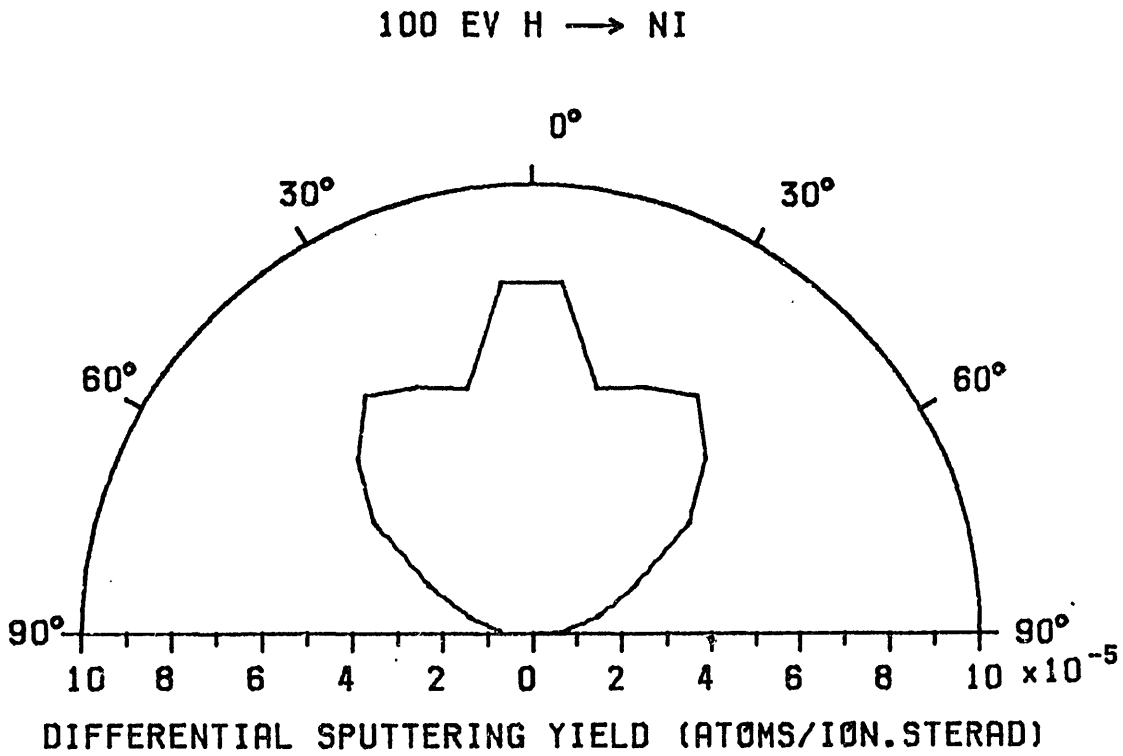
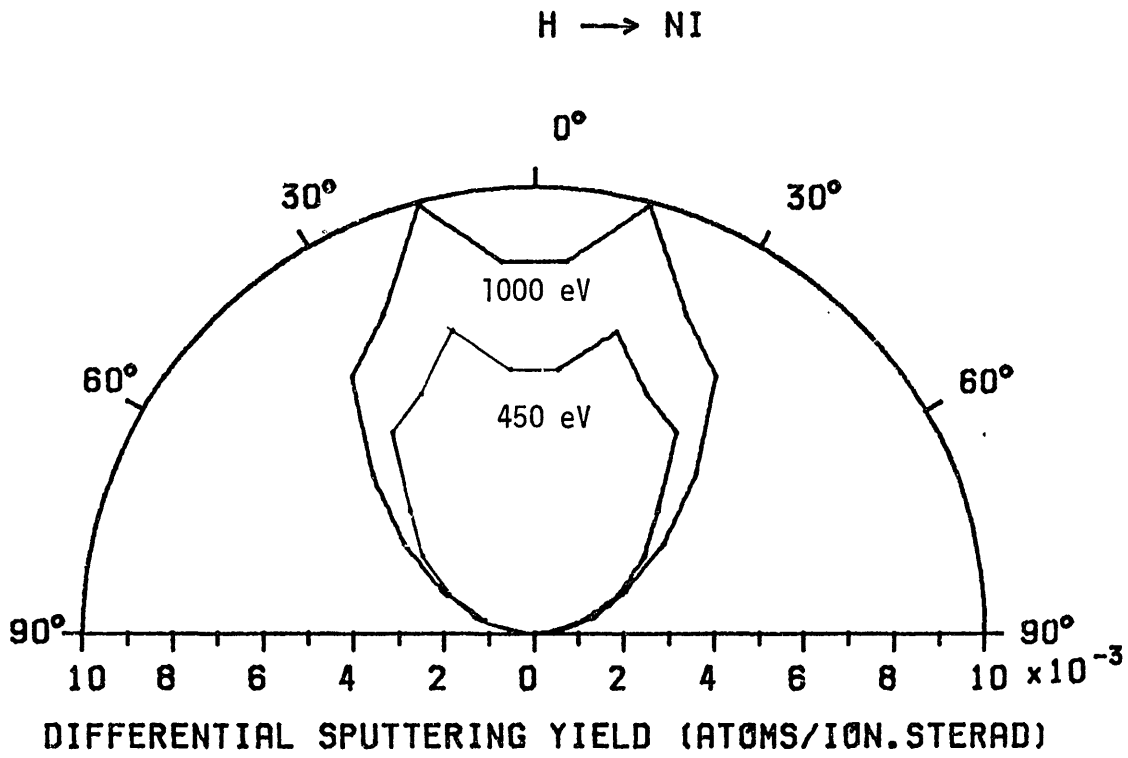


Fig. 19 The angular distributions of sputtered atoms for $H^+ \rightarrow Ni$ at normal incidence

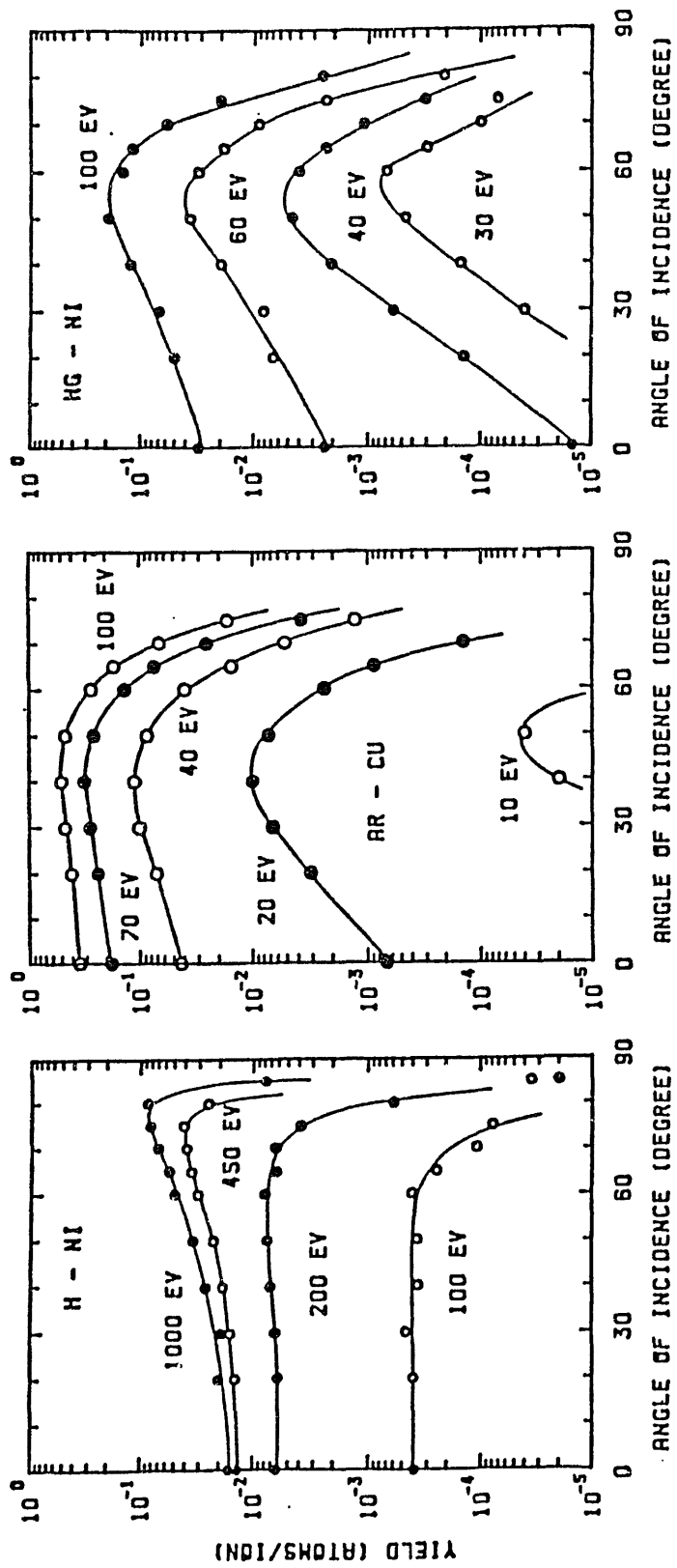


Fig. 20 The bombarding angle dependence of sputtering yields calculated by the ACAT code

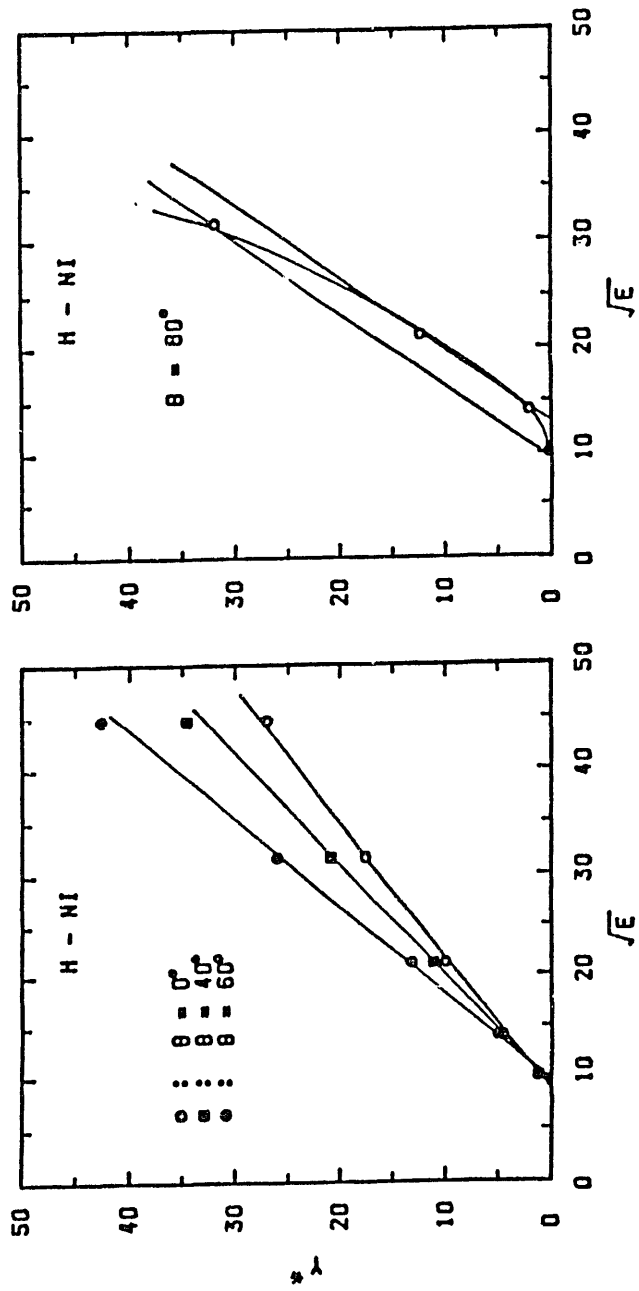


Fig. 21 Y^* of ACAT data plotted as a function of $E^{1/2}$ for
oblique incidence

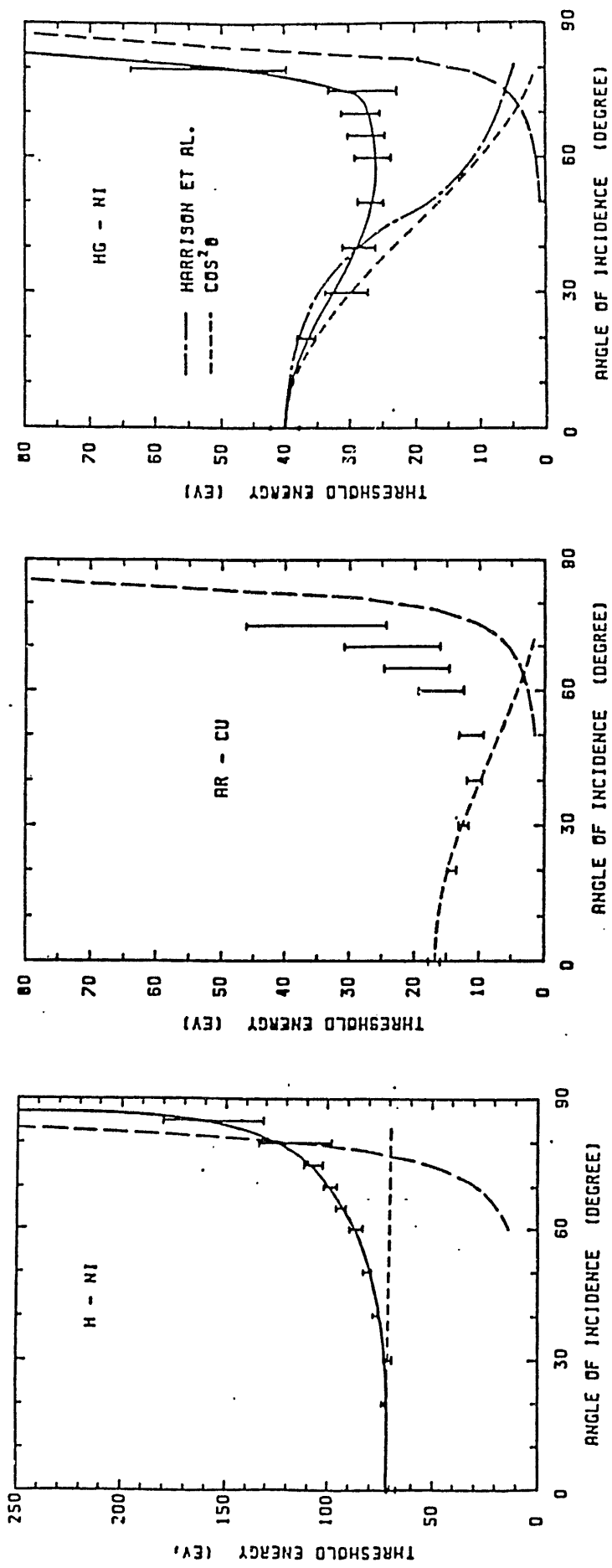


Fig. 22 The bombarding-angle dependence of threshold energies for various ion-target combinations

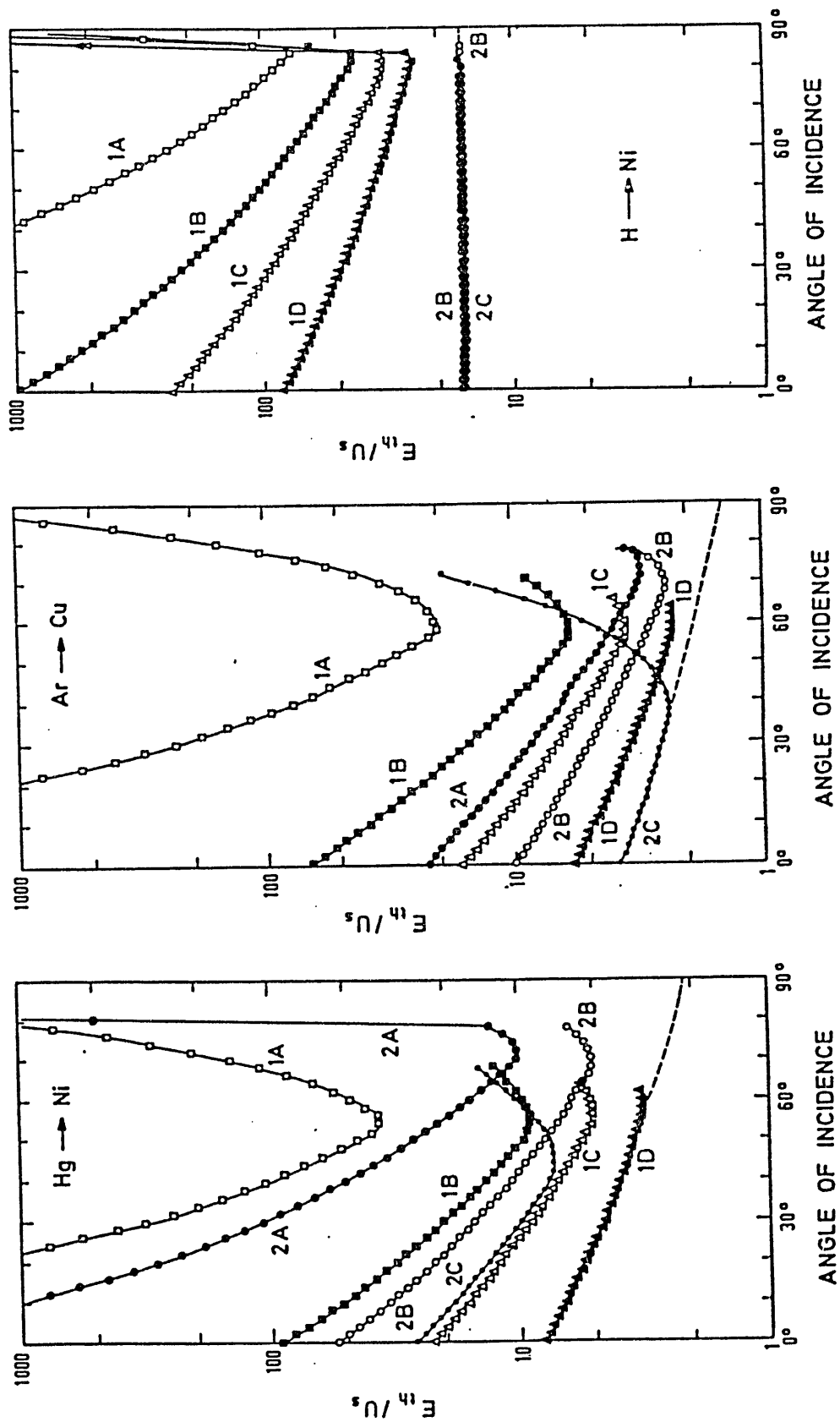


Fig. 23 The theoretical relative threshold energies of different mechanisms as a function of angle of incidence for Hg + Ni, Ar + Cu, and H + Ni combinations

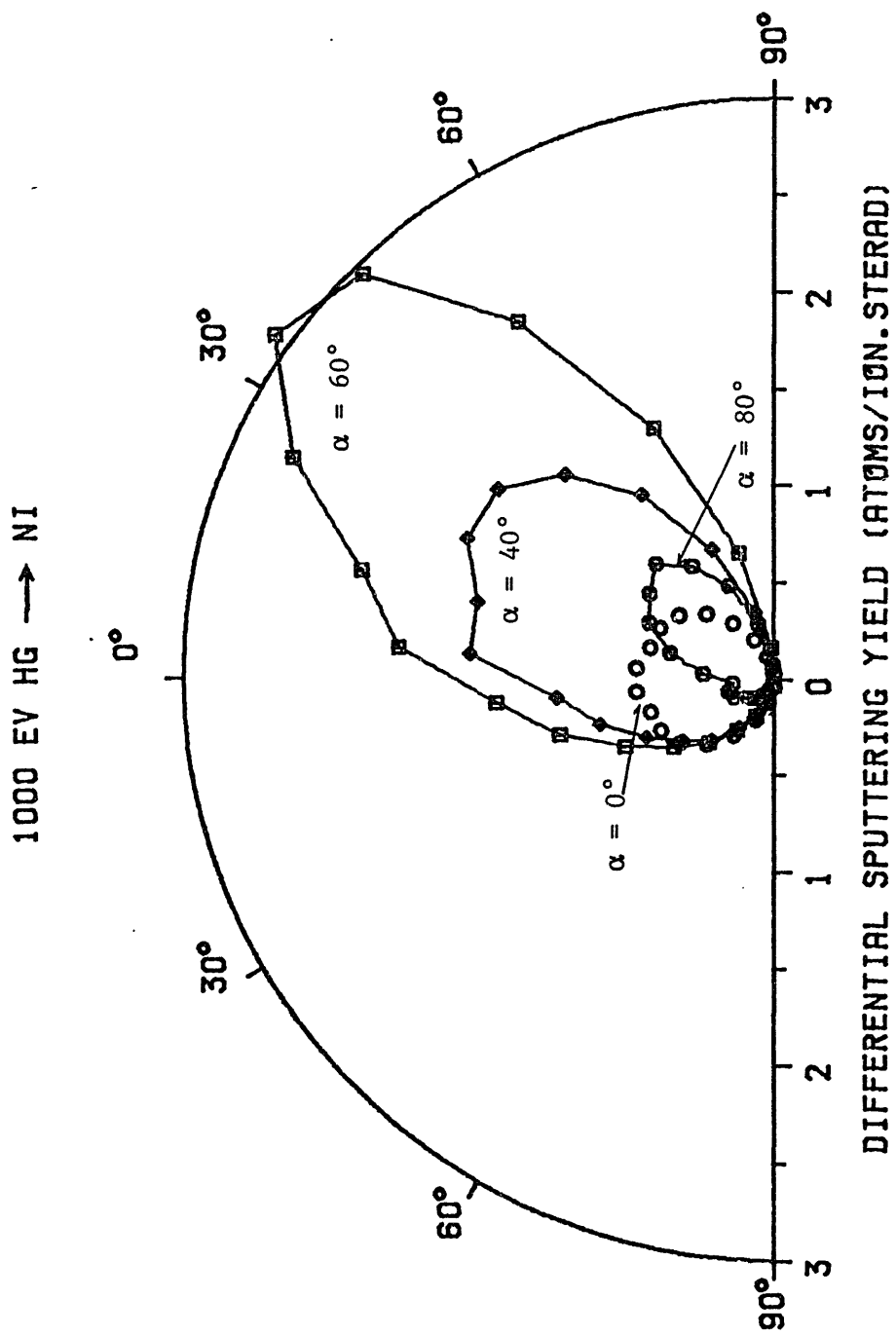


Fig. 24 The ACAT angular distributions of sputtered atoms at different angles of incidence for 1000eV Hg \rightarrow Ni.

100 EV HG \rightarrow NI

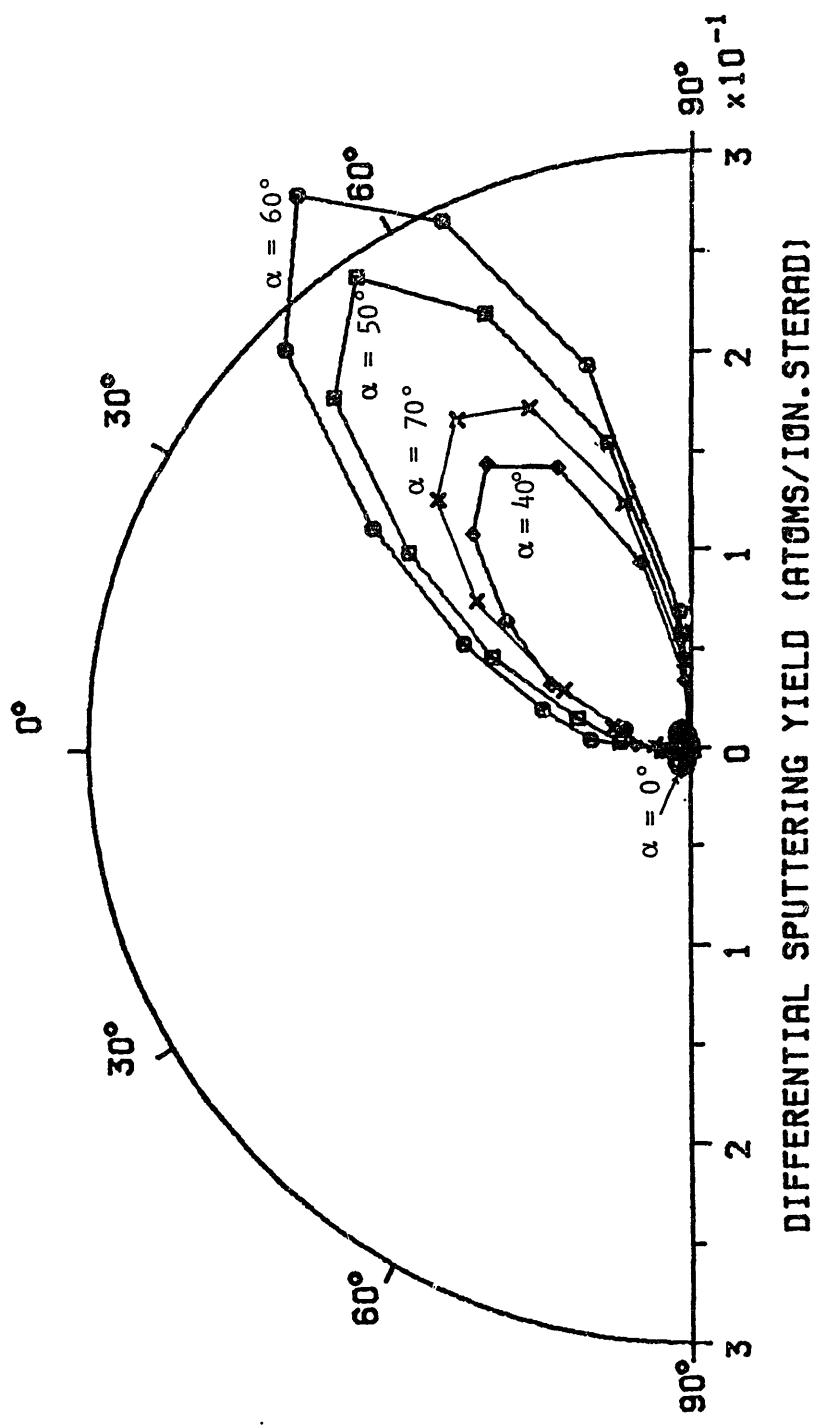


Fig. 25 The ACAT angular distributions of sputtered atoms at different angles of incidence for 100eV Hg \rightarrow Ni.

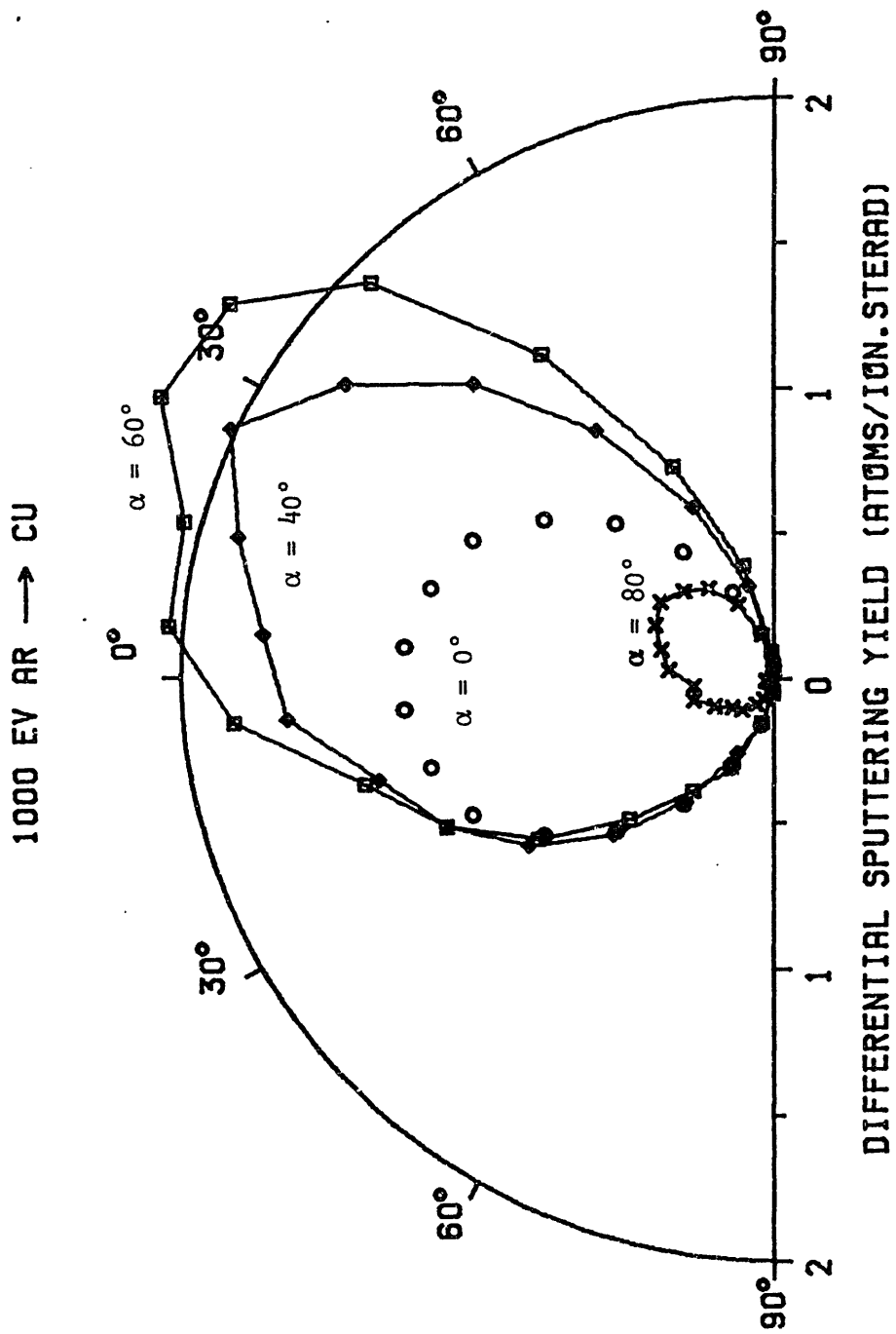


Fig. 26 The ACAT angular distributions of sputtered atoms at different angles of incidence for 1000eV Ar \rightarrow Cu.

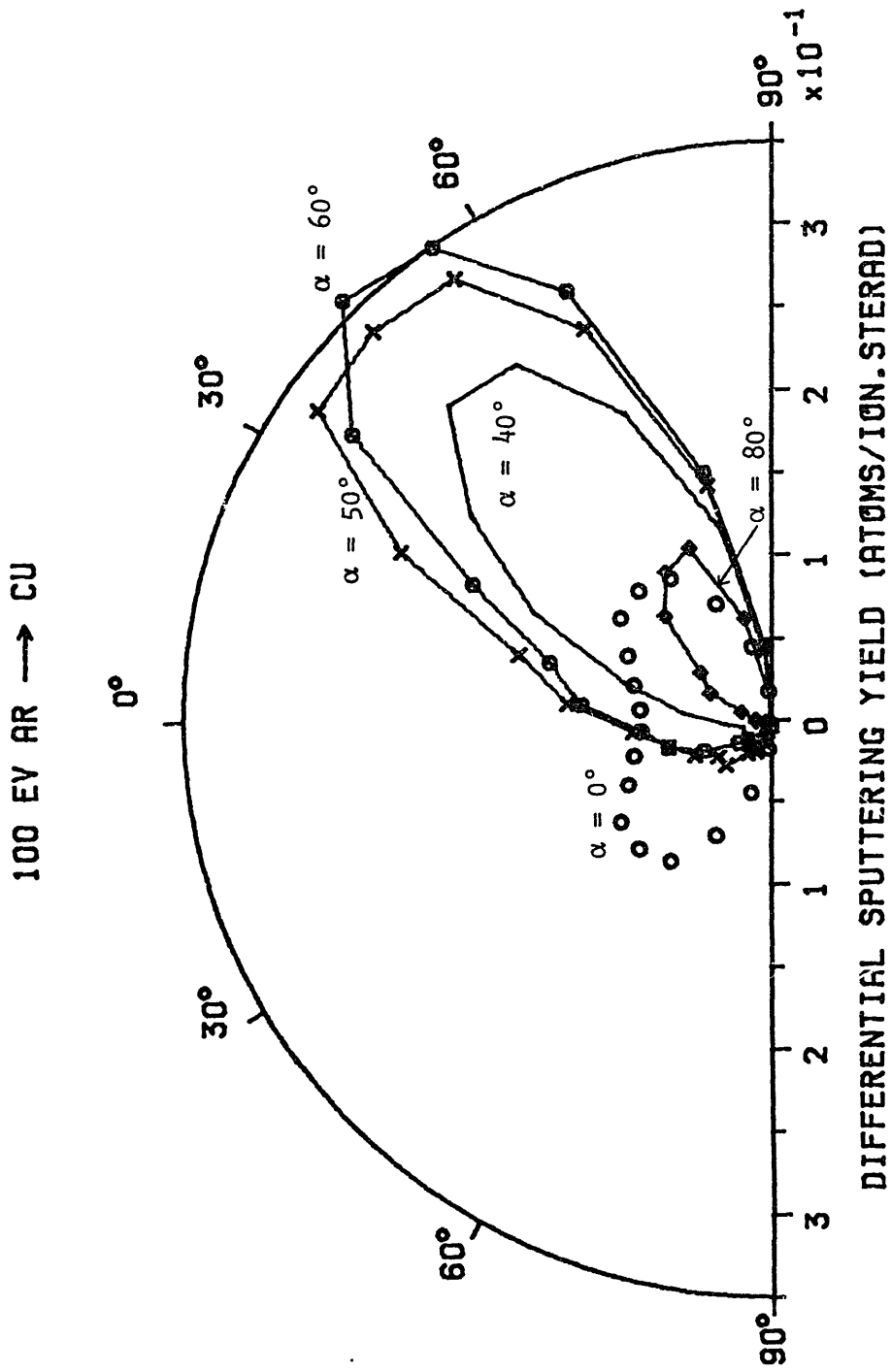


Fig. 27 The ACAT angular distributions of sputtered atoms at different angles of incidence for 100eV Ar \rightarrow Cu.

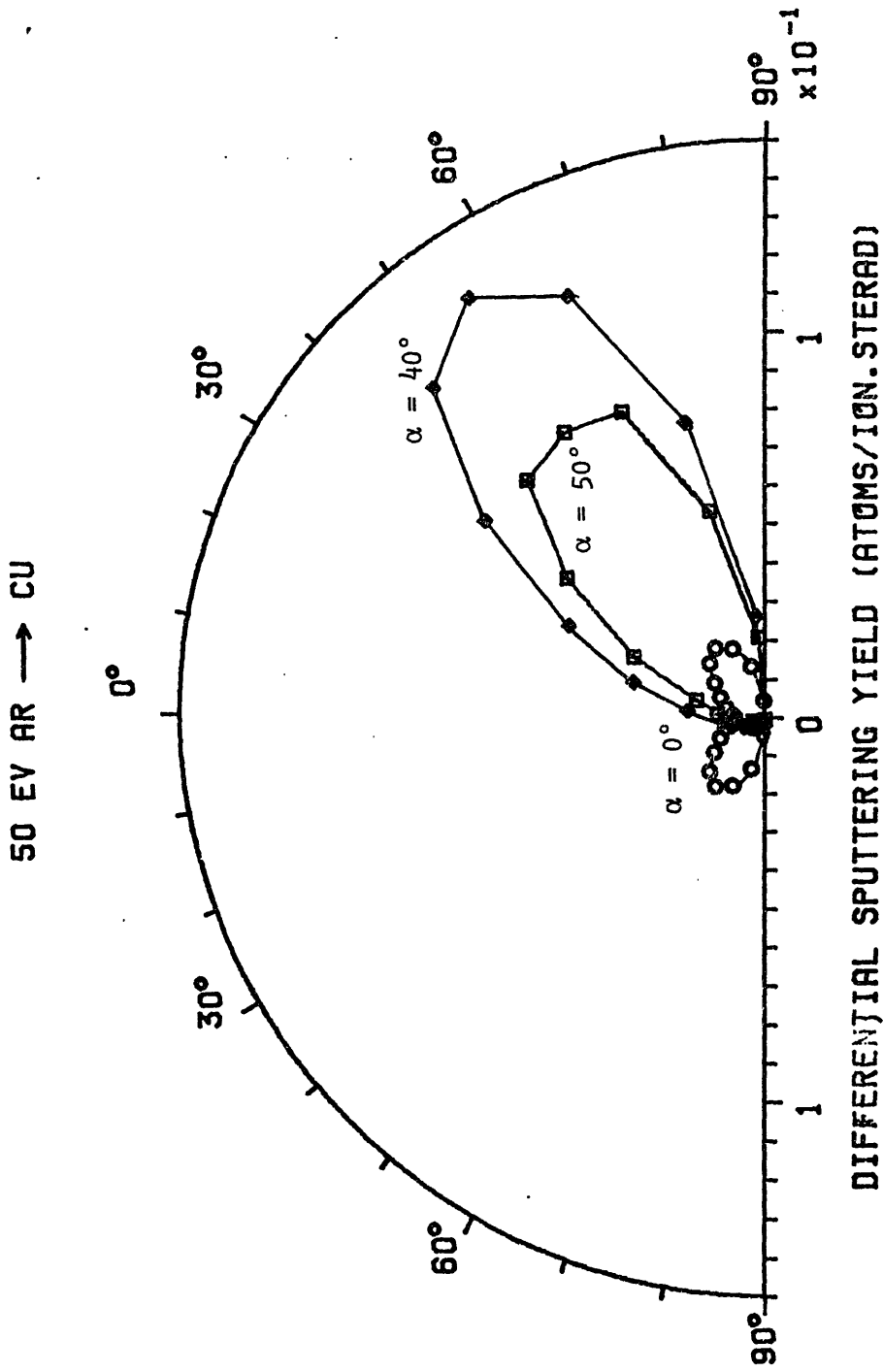


Fig. 28 The ACAT angular distributions of sputtered atoms at different angles of incidence for 50eV Ar \rightarrow Cu.

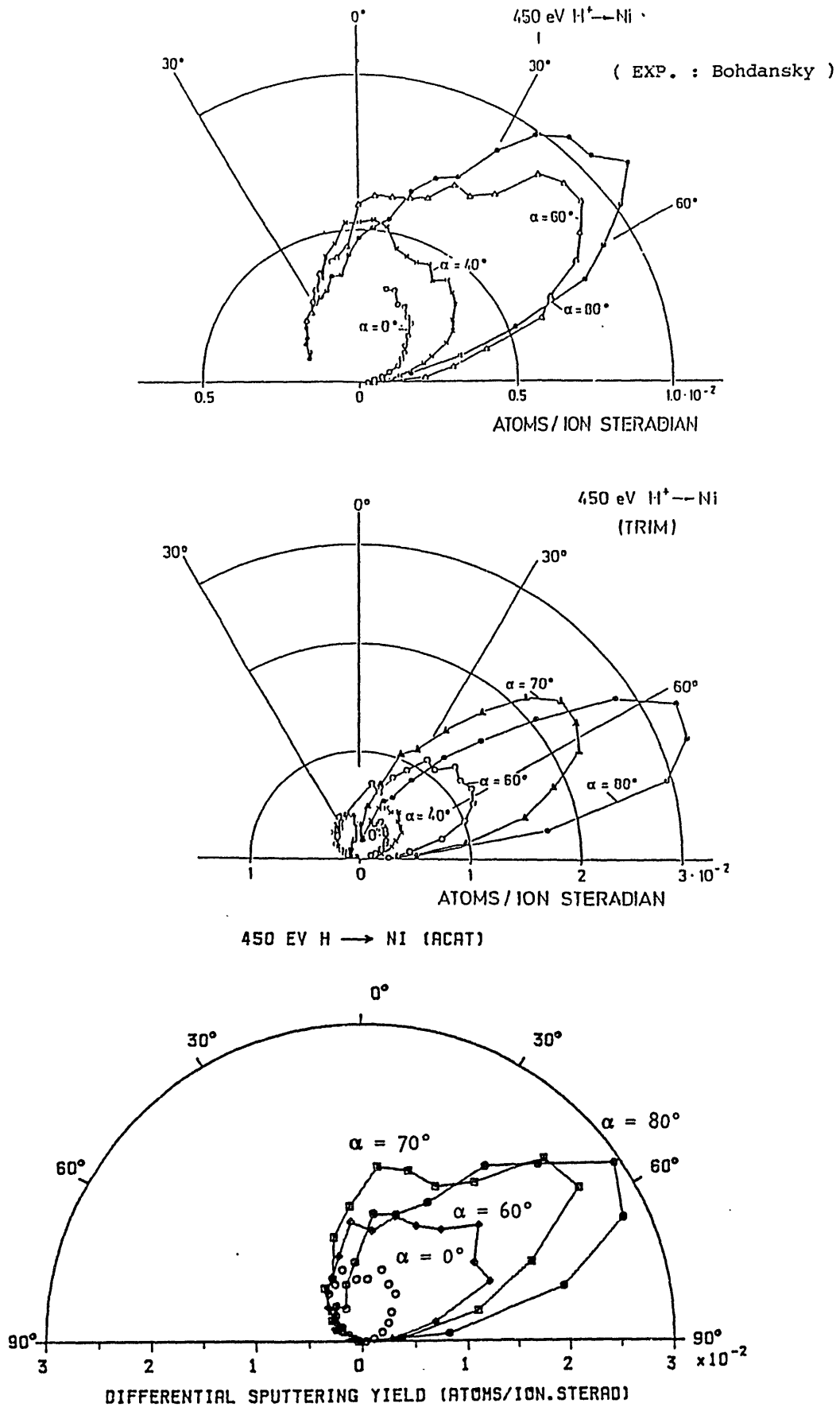
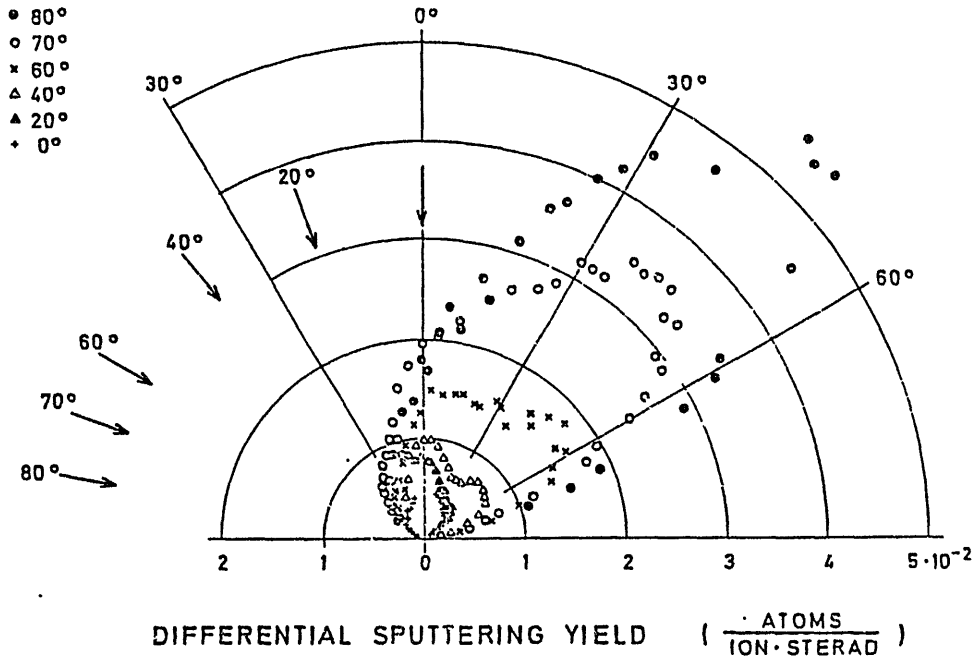


Fig. 29 Comparison of the ACAT angular distributions with the TRIM results and measured distributions in the case of 450eV H → Ni.

3 keV $H_3^+ \rightarrow Ni$

(EXP. : Roth et al.)



1000 EV H \rightarrow NI (ACAT)

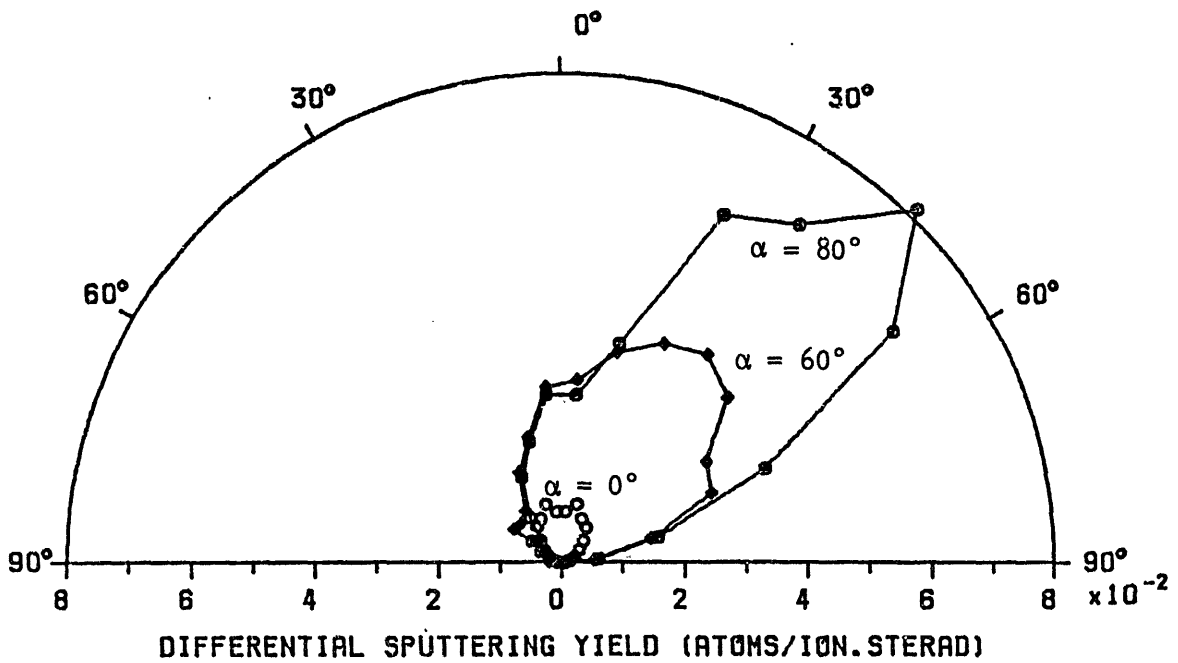


Fig. 30 Comparison of the ACAT angular distributions with the measured results for 1000eV H \rightarrow Ni.

450 EV H → NI

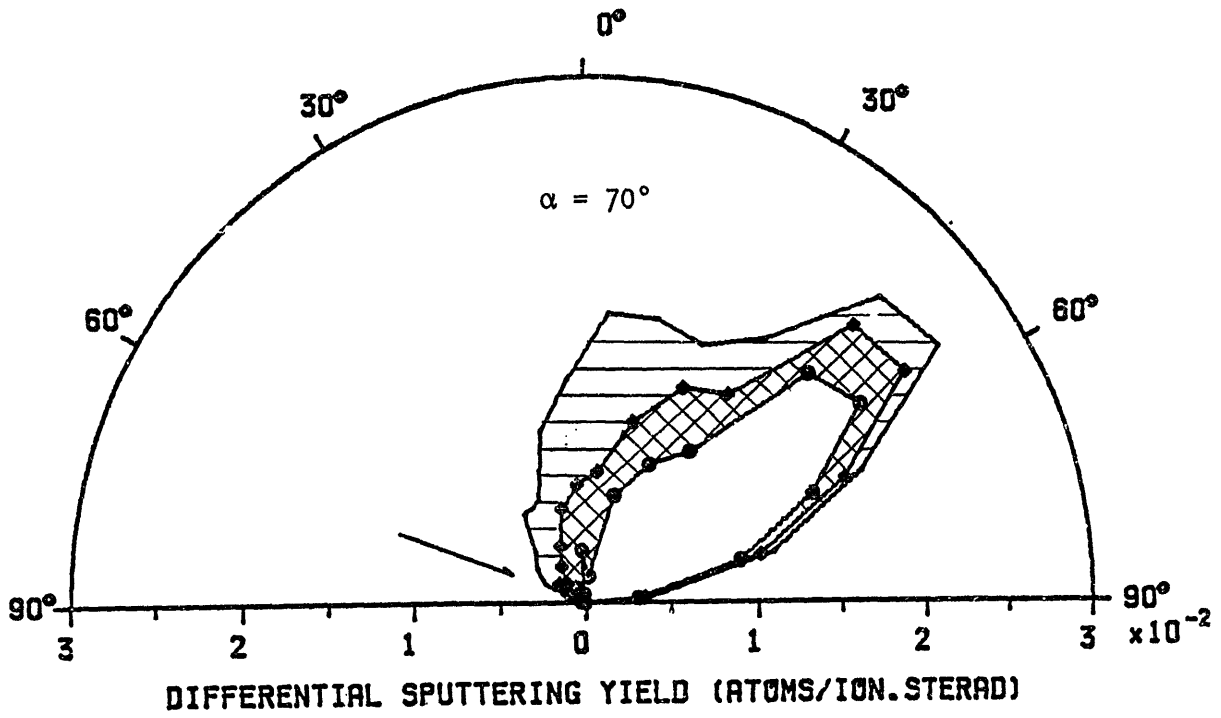


Fig. 31 The contributions of reflected ions to the angular distributions in the case of the oblique incidence of 450eV on Ni target, where the angle of incidence is 70° .

LIST OF IPPJ-AM REPORTS

- IPPJ-AM-1* "Cross Sections for Charge Transfer of Hydrogen Beams in Gases and Vapors in the Energy Range 10 eV –10 keV"
H. Tawara (1977) [Published in Atomic Data and Nuclear Data Tables 22, 491 (1978)]
- IPPJ-AM-2* "Ionization and Excitation of Ions by Electron Impact –Review of Empirical Formulae–"
T. Kato (1977)
- IPPJ-AM-3 "Grotrian Diagrams of Highly Ionized Iron FeVIII-FeXXVI"
K. Mori, M. Otsuka and T. Kato (1977) [Published in Atomic Data and Nuclear Data Tables 23, 196 (1979)]
- IPPJ-AM-4 "Atomic Processes in Hot Plasmas and X-Ray Emission"
T. Kato (1978)
- IPPJ-AM-5* "Charge Transfer between a Proton and a Heavy Metal Atom"
S.Hiraide, Y. Kigoshi and M. Matsuzawa (1978)
- IPPJ-AM-6* "Free-Free Transition in a Plasma –Review of Cross Sections and Spectra–"
T. Kato and H. Narumi (1978)
- IPPJ-AM-7* "Bibliography on Electron Collisions with Atomic Positive Ions: 1940 Through 1977"
K. Takayanagi and T. Iwai (1978)
- IPPJ-AM-8 "Semi-Empirical Cross Sections and Rate Coefficients for Excitation and Ionization by Electron Collision and Photoionization of Helium"
T. Fujimoto (1978)
- IPPJ-AM-9 "Charge Changing Cross Sections for Heavy-Particle Collisions in the Energy Range from 0.1 eV to 10 MeV I. Incidence of He, Li, Be, B and Their Ions"
Kazuhiko Okuno (1978)
- IPPJ-AM-10 "Charge Changing Cross Sections for Heavy-Particle Collisions in the Energy Range from 0.1 eV to 10 MeV II. Incidence of C, N, O and Their Ions"
Kazuhiko Okuno (1978)
- IPPJ-AM-11 "Charge Changing Cross Sections for Heavy-Particle Collisions in the Energy Range from 0.1 eV to 10 MeV III. Incidence of F, Ne, Na and Their Ions"
Kazuhiko Okuno (1978)
- IPPJ-AM-12* "Electron Impact Excitation of Positive Ions Calculated in the Coulomb-Born Approximation –A Data List and Comparative Survey–"
S. Nakazaki and T. Hashino (1979)
- IPPJ-AM-13 "Atomic Processes in Fusion Plasmas – Proceedings of the Nagoya Seminar on Atomic Processes in Fusion Plasmas Sept. 5-7, 1979"
Ed. by Y. Itikawa and T. Kato (1979)
- IPPJ-AM-14 "Energy Dependence of Sputtering Yields of Monatomic Solids"
N. Matsunami, Y. Yamamura, Y. Itikawa, N. Itoh, Y. Kazumata, S. Miyagawa, K. Morita and R. Shimizu (1980)

- IPPJ-AM-15 "Cross Sections for Charge Transfer Collisions Involving Hydrogen Atoms"
Y. Kaneko, T. Arikawa, Y. Itikawa, T. Iwai, T. Kato, M. Matsuzawa,
Y. Nakai, K. Okuno, H. Ryufuku, H. Tawara and T. Watanabe (1980)
- IPPJ-AM-16 "Two-Centre Coulomb Phaseshifts and Radial Functions"
H. Nakamura and H. Takagi (1980)
- IPPJ-AM-17 "Empirical Formulas for Ionization Cross Section of Atomic Ions for
Electron Collisions –Critical Review with Compilation of Experimental
Data–"
Y. Itikawa and T. Kato (1981)
- IPPJ-AM-18 "Data on the Backscattering Coefficients of Light Ions from Solids"
T. Tabata, R. Ito, Y. Itikawa, N. Itoh and K. Morita (1981)
- IPPJ-AM-19 "Recommended Values of Transport Cross Sections for Elastic Collision and
Total Collision Cross Section for Electrons in Atomic and Molecular Gases"
M. Hayashi (1981)
- IPPJ-AM-20 "Electron Capture and Loss Cross Sections for Collisions between Heavy
Ions and Hydrogen Molecules"
Y. Kaneko, Y. Itikawa, T. Iwai, T. Kato, Y. Nakai, K. Okuno and H. Tawara
(1981)
- IPPJ-AM-21 "Surface Data for Fusion Devices – Proceedings of the U.S.–Japan Work-
shop on Surface Data Review Dec. 14-18, 1981"
Ed. by N. Itoh and E.W. Thomas (1982)
- IPPJ-AM-22 "Desorption and Related Phenomena Relevant to Fusion Devices"
Ed. by A. Koma (1982)
- IPPJ-AM-23 "Dielectronic Recombination of Hydrogenic Ions"
T. Fujimoto, T. Kato and Y. Nakamura (1982)
- IPPJ-AM-24 "Bibliography on Electron Collisions with Atomic Positive Ions: 1978
Through 1982 (Supplement to IPPJ-AM-7)"
Y. Itikawa (1982)
- IPPJ-AM-25 "Bibliography on Ionization and Charge Transfer Processes in Ion-Ion
Collision"
H. Tawara (1983)
- IPPJ-AM-26 "Angular Dependence of Sputtering Yields of Monatomic Solids"
Y. Yamamura, Y. Itikawa and N. Itoh (1983)
- IPPJ-AM-27 "Recommended Data on Excitation of Carbon and Oxygen Ions by Electron
Collisions"
Y. Itikawa, S. Hara, T. Kato, S. Nakazaki, M.S. Pindzola and D.H. Crandall
(1983)
- IPPJ-AM-28 "Electron Capture and Loss Cross Sections for Collisions Between Heavy
Ions and Hydrogen Molecules (Up-dated version of IPPJ-AM-20)
H. Tawara, T. Kato and Y. Nakai (1983)

- IPPJ-AM-29 "Bibliography on Atomic Processes in Hot Dense Plasmas"
T. Kato, J. Hama, T. Kagawa, S. Karashima, N. Miyanaga, H. Tawara, N. Yamaguchi, K. Yamamoto and K. Yonei (1983)
- IPPJ-AM-30 "Cross Sections for Charge Transfers of Highly Ionized Ions in Hydrogen Atoms (Up-dated version of IPPJ-AM-15)"
H. Tawara, T. Kato and Y. Nakai (1983)
- IPPJ-AM-31 "Atomic Processes in Hot Dense Plasmas"
T. Kagawa, T. Kato, T. Watanabe and S. Karashima (1983)
- IPPJ-AM-32 "Energy Dependence of the Yields of Ion-Induced Sputtering of Monatomic Solids"
N. Matsunami, Y. Yamamura, Y. Itikawa, N. Itoh, Y. Kazumata, S. Miyagawa, K. Morita, R. Shimizu and H. Tawara (1983)
- IPPJ-AM-33 "Proceedings on Symposium on Atomic Collision Data for Diagnostics and Modelling of Fusion Plasmas, Aug. 29 – 30, 1983"
Ed. by H. Tawara (1983)
- IPPJ-AM-34 "Dependence of the Backscattering Coefficients of Light Ions upon Angle of Incidence"
T. Tabata, R. Ito, Y. Itikawa, N. Itoh, K. Morita and H. Tawara (1984)
- IPPJ-AM-35 "Proceedings of Workshop on Synergistic Effects in Surface Phenomena Related to Plasma-Wall Interactions, May 21 – 23, 1984"
Ed. by N. Itoh, K. Kamada and H. Tawara (1984)
- IPPJ-AM-36 "Equilibrium Charge State Distributions of Ions ($Z_1 \geq 4$) after Passage through Foils – Compilation of Data after 1972"
K. Shima, T. Mikumo and H. Tawara (1985)
- IPPJ-AM-37 "Ionization Cross Sections of Atoms and Ions by Electron Impact"
H. Tawara, T. Kato and M. Ohnishi (1985)
- IPPJ-AM-38 "Rate Coefficients for the Electron-Impact Excitations of C-like Ions"
Y. Itikawa (1985)
- IPPJ-AM-39 "Proceedings of the Japan-U.S. Workshop on Impurity and Particle Control, Theory and Modeling, Mar. 12 – 16, 1984"
Ed. by T. Kawamura (1985)
- IPPJ-AM-40 "Low-Energy Sputterings with the Monte Carlo Program ACAT"
Y. Yamamura and Y. Mizuno (1985)

Available upon request to Research Information Center, Institute of Plasma Physics, Nagoya University, Nagoya 464, Japan, except for the reports noted with*.

